The Dissertation Committee for Melissa Anne Frei

certifies that this is the approved version of the following dissertation:

Comparative Efficiency and Parameter Recovery of Spin Aligned Templates for Compact Binary Coalescence Detection

Committee:

Richard Matzner, Supervisor

Christina Markert

Milos Milosavljevic

Sacha Kopp

Duane Dicus

Comparative Efficiency and Parameter Recovery of Spin Aligned Templates for Compact Binary Coalescence Detection

by

Melissa Anne Frei, B.S.

Dissertation

Presented to the Faculty of the Graduate School of

The University of Texas at Austin

in Partial Fulfillment

of the Requirements

for the Degree of

Doctor of Philosophy

The University of Texas at Austin

August 2011

Dedicated to my late father who taught me to look up at the sky with wonder, awe and a critical mind. To my family and friends who supported me through the long haul. To my mother whose generosity reduced my daily stress. To my brother and sister-in-law for never letting me forget the joy of normal life. To my good friends, too numerous to mention here, who always listened to me when life was overwhelming. Of course to the office couch for its many refreshing naps.

Special thanks to those who gave me the opportunities and the help I needed to complete this project and to my collaborators Kipp Cannon, Chad Hanna, Drew Keppel, Leo Singer, and Alan Weinstein. Also thanks to those who wrote both LAL and gstlal not already named above. Thanks to those in the NINJA2 collaboration who efforts produced the datasets used in this dissertation.

Comparative Efficiency and Parameter Recovery of Spin Aligned Templates for Compact Binary Coalescence Detection

Publication No. _____

Melissa Anne Frei, Ph.D.
The University of Texas at Austin, 2011

Supervisor: Richard Matzner

Compact binary coalescing systems: binary neutron stars, neutron star black hole pairs and binary black hole systems, represent promising candidates for gravitational wave first detection and have the potential to provide precise tests of the strong-field predictions of general relativity. Observations of binary black hole (BBH) systems will provide a wealth of information relevant to fundamental physics, astrophysics and cosmology. The search for such systems is a major priority of the Laser Interferometer Gravitational-Wave Observatory (LIGO) and Virgo collaborations. A major area of research within LIGO-Virgo

analysis groups is incorporation of spin into the search template banks used for binary black hole systems. In this dissertation, I compare the injection efficiency and parameter recovery from three binary black hole searches. One of the searches presented here uses non-spinning templates and represents the standard LIGO search for binary black holes with total masses between 35 and $100M_{\odot}$, [40]. The other two use spin aligned and anti-aligned templates representing a future search for black hole binary systems with total masses between 35-$100M_{\odot}$. One of the two spinning searches has the spin parameter set to zero, nonspinning, as a check of the spinning method. (Additionally the (anti-)aligned spin searches use a retooling of the standard pipeline taking advantage of a code base designed specifically to handle Advanced LIGO data.) All three searches were run on artificial data created by the *Numerical Injection Analysis 2* collaboration (*NINJA2*) containing Gaussian noise and numerically generated signals modeling aligned and anti-aligned spinning binary black holes, [71]. I found that for the analyzed two weeks of data the three searches recover injections with nearly equal efficiency; however, the spinning search recovers the parameters of the injections more accurately than the non-spinning search. Specifically, the parameter recovery of the spins shows a correlation between the injected and recovered spins, and the addition of spin to the template bank improves the recovery of the signal-to-noise ratio and the chirp mass for an injected signal. While spin aligned situations are geometrically low probability configurations, there are plausible astrophysical effects that lead to alignment of spins prior to merger, [72, 77, 80]. Therefore my results show that the spin-aligned template bank search represents an improvement on the standard non-spinning search in the highmass region and should be pursued on real data.

Contents

Abstract v

List of Figures viii

Chapter 1 Overview 1

1.1 Conventions and Definitions Used In This Dissertation 4

1.2 Gravitational Waves in General Relativity 8

1.3 Linearized Gravity and Gravitational Waves 9

1.4 An Overview of Gravitational Wave Astronomy With LIGO . 14

Chapter 2 Gravitational Wave Modeling 18

2.1 An Overview of Post Newtonian Formalisms 19

2.2 Basic Numerical Relativity Techniques 21

2.3 Hybrid Techniques 23

2.3.1 Inspiral Merger and Ringdown Waveforms 24

2.3.2 Inspiral Merger and Ringdown Spin Aligned Waveforms 27

2.4 NINJA2 32

Chapter 3 *gstlal* **34**

3.1 General Pipeline Structures 34

3.2 Matched Filtering 39

3.3 Singular Value Decomposition and *gstlal* 40

Chapter 4 IMRSA Template Banks **43**

4.1 The Distribution of Templates Used 44

4.2 Template Bank Simulations 45

Chapter 5 Results and Conclusions **52**

5.1 Results 53

5.1.1 Comparative Efficiencies 53

5.1.2 Parameter Recovery 59

5.2 Conclusions 65

Bibliography **67**

Vita **78**

List of Figures

1.1 LIGO's best strain sensitivities for the first five science runs, [56]. 15

1.2 The general layout of a LIGO interferometer (the laser power numbers here are generic; specific power levels are given in Table 1 of [8]). 17

2.1 A spinning IMRSA waveform with: total mass $20M_{\odot}$, $q = m_1/m_2 = 1$ and $\chi = -0.85$, illustrating the different stages of the waveform: inspiral, merger, and ringdown. 20

2.2 An illustration of the relation between time slices in the ADM formalism. n_a is a unit time like normal to the slice. t_a is the direction of flow of the time coordinate in the chosen coordinate system. Image is from [45] 22

2.3 A cartoon showing the relation between conponent spins, $\vec{S}_i$, and orbital spin, $\vec{L}$, in the anti-aligned case. 26

3.1 A schematic depicting the organization of the ihope search, adapted from [19]. 37

3.2 A schematic depicting the organization of the lloid search pipeline, [70]. In lloid the data are collected, weighted by a function containing information about the power spectral density of the detector at that time, and then the template banks are generated. The templates are then sliced and resampled so that spectral regions with lower frequency are sampled with fewer points. For each sampling rate, the SVD is calculated, see section 3.3, and the resulting *singular values* are thresholded on at the gate and reassembled into the SNR stream. 38

4.1 The first plot shows the distribution of templates in the m_1-m_2 plane; the second, shows the distribution in the χ-q plane. . . 46

4.2 Representative plot of the overlap between the template bank and 10 random injections; specifically, the results from injection six in Table 4.1. The injection is shown as a star inside a box on the plot. The other points in the graph are from the IMRSA template bank generated in the method described above. The plot shows that in the m_1-m_2 plane the injection has high overlaps, indicated by circles of dark red color, with templates near to it. 50

4.3 Representative plot of the overlap between the template bank and 10 random injections; specifically, the results from injection six in Table 4.1. The injection is shown as a star inside a box on the plot. The other points in the graph are from the IMRSA template bank generated in the method described above. The plot shows that in the χ-q plane the injection has high overlaps with templates within a range of about 1.0 around the injected χ value, with better placement schemes this window may be reduced. 51

5.1 The found-missed plot for the injections displaying the chirp mass of the injection on the x-axis and the effective distance of the injection on the y-axis. The top plot is for *L1* from the spinning IMRSA template bank search. The bottom plot is for *V1* from the spinning IMRSA template bank search. The empty circles are the missed injections. The crosses are the found injections. This search is compared to the nonspinning highmass search. The filled circles represent injections found by the standard non- spinning highmass search and missed by the spinning IMRSA template bank search. *H1* results are omitted as the two searches were equally efficient. 57

5.2 The found-missed plot for the injections displaying the chirp mass of the injection on the x-axis and the effective distance of the injection on the y- axis. The top plot is for *L1* from the spinning IMRSA search. The bottom for *V1* from the spinning IMRSA search. The empty circles are the missed injections. The crosses are the found injections. This search is compared to the nonspinning IMRSA search. In the top plot the filled square is an injection found by the spinning IMRSA template bank search but missed by the nonspinning IMRSA template bank search. In the bottom the filled circle is an injection missed by the spinning IMRSA template bank search but found by the nonspinning IMRSA template bank search. *H1* results are omitted as the two searches were equally efficient. 58

5.3 The SNR recovery: top, the spinning IMRSA template bank search; middle, the nonspinning highmass search; bottom the nonspinning IMRSA template bank search. Only *H1* results are shown as the results in *L1* and *V1* show the same improvements as seen in *H1*. 62

5.4 The mchirp recovery: top, the spinning IMRSA template bank search; middle, the nonspinning highmass search; bottom the nonspinning IMRSA template bank search. Only results from *H1* are shown. The same improvements are seen in all three interferometers. 63

5.5 The combined spin, χ, recovery from the spinning IMRSA template bank search. The same correlation is seen in all three detectors so only the *H1* results are shown. 64

Chapter 1

Overview

Gravitational waves are described by general relativity. They are generated by the asymmetric movement of masses. While many systems involve the asymmetric movement of masses, most produce waves too faint to be detected by instruments like the amplitude detectors of the Laser Interferometer Gravitational-Wave Observatory (LIGO). The amplitude of a gravitational wave falls off as r^{-1}, the inverse of the distance to the source, so whether a source is detected depends on the amplitude of the emission and on r. Types of signals potentially visible to LIGO are compact binary coalescence (CBC) sources such as binary neutron star and binary black hole systems. The signal is produced as the compact binary objects lose orbital energy to gravitational radiation, spiral in, and eventually collide and coalesce.

This dissertation focuses on binary black hole (BBH) systems with masses between 35-100 $M_{\odot}$. Black holes observed in X-ray binaries have masses ranging only up to about 20 $M_{\odot}$. Population-synthesis models indicate that

the typical masses of the component black holes for systems evolving to merger within the 10 Gyr range, roughly the age of the universe, is from 5 to 10 $M_{\odot}$, [28, 39, 73, 74, 78, 86], but it has been suggested that more massive systems can be formed by isolated stellar evolution producing component masses on the order of 20 $M_{\odot}$, [79]. Models of very low metallicity stellar evolution suggest the possibility of very massive stars with a chance of producing black holes with masses greater than $35M_{\odot}$, [47, 48]. Also it seems probable that dynamical interactions can produce black holes in the 35-100 $M_{\odot}$ range. A heavier black hole will fall to the center of a dense cluster where it can replace a smaller mass black hole in a pre-existing binary through three-body interactions resulting in a tighter-bound binary leading to an eventual merger after the ejection of the smaller black hole. This process may happen several times generating a final black hole in the 35-100$M_{\odot}$ range, [5].

The efforts to find gravitational wave signals from CBC systems of any type in detectors like LIGO require *template* based searches. Such searches measure the correlation between the detector data stream and analytically described waveforms known as *templates*. When that correlation exceeds a predetermined threshold a *trigger*, potential signal, is said to occur. Templates are analytical models of gravitational waves requiring foreknowledge of the evolution of the source.

In the last decade leaps have been made in modeling gravitational waves from CBC sources. The iterative techniques of numerical relativity have been used to generate templates of waveforms covering the life cycle of a binary black

hole. The waveforms span from the chirp, generated by the early *inspiral* of the two bodies, to their *merger* and the transition to the *ringdown* of the final mass, when the system becomes stationary as a result of the damping provided by the emitted gravitational waves. Inherent limitations exist for generating complete waveforms by either analytical or computational techniques.

Signals from lowmass binaries, like binary neutron stars, can sweep through the LIGO sensitivity range before their merger begins, so it is only necessary to model the inspiral for such systems. Other systems, like higher mass binary black holes, have merger frequencies within the sensitivity limits of LIGO. Therefore templates containing the complete waveform are valuable to the current detectors, especially for binary black holes where the majority of the signal's power is contained in the later stages of the waveform. For binary black holes, templates modeling the complete gravitational wave are made from waveforms composed of post-Newtonian inspiral and numerically generated mergers and ringdown.

The CBC analysis group in the LIGO Virgo Collaboration (LVC) is continually developing better template families to search for possible astrophysical signals in the detector's respective data streams. One important area of development is producing templates modeling waveforms generated by binary black hole systems containing one or two spinning bodies since the majority of CBC sources are expected to have spin. Current LIGO CBC searches include only non-spinning signals and are expected to miss a large number of incoming signals, [65]. In this dissertation, I will use a matched filter technique

for gravitational wave analysis, [26], to investigate the use of a restricted set of spinning templates to detect computationally generated signals describing spinning sources in Gaussian noise.

Many new templates are currently being investigated for use in a spinning search. One family includes IMR (inspiral, merger, ringdown) waveforms for aligned or anti-aligned spinning sources in the highmass range, 35-100$M_{\odot}$. This dissertation examines the ability of these IMR spin aligned (IMRSA) templates to detect numerically generated signals produced by the numerical injection analysis 2 (NINJA2) project for sources with aligned or anti-aligned spins in two weeks of colored Gaussian noise produced by the NINJA2 collaboration, [71]. Significant scientific gains compared to a search without spin would make a search using IMRSA templates the preferred method in the higher mass region. The process of evaluating a template family based on its ability to detect numerical simulations in data, described in this dissertation, will also be applicable to other new template families as they are developed like those described in [58].

1.1 Conventions and Definitions Used In This Dissertation

In this dissertation unless otherwise specified geometrical units are used so that c=G=1. The specification c=1 means that time and length use the same units, e.g. [t]=seconds, [l]=light-second. The specification G=c=1 also means

that the units of mass and length are the same. For instance, the mass of the sun is: $M = M_{\odot} = 1.5km = 0.5 \times 10^{-5} sec.$

Additionally, commas in formulas are to be treated as derivatives. Indices on vector and tensor quantities presented are raised and lowered with the flat metric unless otherwise stated.

Unless otherwise stated all templates discussed in this dissertation are determined by their mass parameters such as m_1 and m_2.

Some terms are standard in the field of LIGO-Virgo data analysis but are often confusing to those not familiar with the field, included here is a short glossary such terms.

- glitch : an event with an SNR over the threshold (5.5) but not a gravitational wave
- hybrid waveform : an analytical waveform made by stitching a post-Newtonian waveform to a numerically generated waveform modeling the later portions of the waveform
- injection : an analytical model of a waveform generally the same as a template. It is used in a search either of real data or of artificial noise as a simulated source to test the pipeline's ability to find signals of the same type as the model. In the NINJA2 search, injections are numerical simulations of gravitational waves. Injections are also used in simulations designed to test how well a template bank covers the given parameter space.

- phenomenological waveforms: analytical waveforms created by fitting to hybrid waveforms
- signal to noise ratio (SNR): defined by (3.2.3), it is the value used to determine if a possible signal is present in the data stream. A SNR above 5.5 is a possible signal, below that value the data stream is considered to contain only noise.
- template : an analytical modeling of a waveform used to find gravitational waves in interferometer data
- waveform : the gravitational wave emitted from the asymmetric movement of massive objects characterized by an amplitude and a phase
- whiten: a de-weighting of signal components with frequencies outside the sensitive bandpass of the detector in LIGO. This is done by dividing the signal by the square root of the noise power spectral decomposition.

Acronyms and abbreviations are used in LIGO commonly, the following is a list of those used in this thesis.

- Banksim = template Bank Simulation
- CBC = Compact Binary Coalescence
- EOB = Effective One Body
- EOBNR = Effective One Body Numerical Relativity

- ETM = End Test Mirror
- gstlal = gstreamer LAL
- highmass = CBC search range for sources between 35 and 100 $M_{\odot}$
- IMR = Inspiral Merger Ringdown
- IMRSA = Inspiral Merger Ringdown Spin-Aligned
- ITM = Inner Test Mass
- LAL = LSC Algorithmic Library
- LIGO = Laser Interferometer Gravitational Wave Observatory
- lloid = low latency online inspiral detection
- lowmass = CBC search range for sources between 1 and 35 $M_{\odot}$
- LSC = LIGO Scientific Collaboration
- LVC = LIGO Virgo Scientific Collaboration
- mchirp = chirp mass
- NR = Numerical Relativity
- PN = Post Newtonian
- PR = Power Recycling mirror
- S5 = LIGO's fifth science run

- SNR = Signal to Noise Ratio
- SVD = Singular Value Decomposition

1.2 Gravitational Waves in General Relativity

The specifics and the mathematics of gravitational waves require general relativity or one of its extensions. Here we consider only standard general relativity.

In special relativity no information can be transferred faster than the speed of light, c, which in geometrical units is 1 and unitless, see Section 1.1. So when massive bodies move, changes in their gravitational field are not known immediately throughout the universe. The information travels at the speed of light, c, as ripples out from the source in the gravitational field known as *gravitational waves*.

General relativity shows that the masses must be moving asymmetrically to produce a gravitational wave, see Section 1.3. Example sources include binary systems undergoing inspiral, merger and ringdown. The binary pulsar PSR 1913+16 is a rapidly rotating neutron star emitting periodic bursts of radio waves and was discovered in our galaxy by Russell Hulse and Joseph Taylor, [44]. PSR 1913+16 has been monitored for several decades and its orbital period has been shown to be decreasing at a rate consistent with energy loss via the emission of gravitational waves predicted by general relativity for a binary neutron star system [44]. PSR1913+16 will take about

300 million years for its component neutron stars to coalesce into a single compact object with only the last few seconds of the inspiral within the LIGO sensitivity range [44]. It is estimated that binary neutron star mergers from sources within a sphere of radius about $200Mpc$ occur with a frequency of a few per year [41]. It is good to remember that neutron star binaries correspond to only one type of compact binary coalescent sources visible to LIGO; other possibilities include the merger of binary black holes, and of black hole neutron star binary systems.

1.3 Linearized Gravity and Gravitational Waves

Several approaches to general relativity illustrate the existence of gravitational waves. Here I present the linearized description of gravity and the quadruploar formulation. The linearized theory begins by assuming space-time to be essentially flat and all corrections to the flat metric, Equation (1.3.1), can be contained in one term, $h_{\mu\nu}$ so that $g_{\mu\nu} = \eta_{\mu\nu} + h_{\mu\nu}$. The theory is called linearized because higher order corrections like $h^2_{\mu\nu}, h^3_{\mu\nu}, h^4_{\mu\nu} \cdots$ are taken to be small enough to be safely ignored. For the linearized metric the connection coefficients, $\Gamma^{\mu}_{\alpha\beta}$, are defined by Equation (1.3.2) and the Ricci tensor, $R_{\mu\nu}$, is given by Equation (1.3.3).

$$\eta_{\mu\nu} = \begin{bmatrix} -1 & 0 & 0 & 0 \\ 0 & 1 & 0 & 0 \\ 0 & 0 & 1 & 0 \\ 0 & 0 & 0 & 1 \end{bmatrix} \tag{1.3.1}$$

$$\Gamma^{\mu}_{\alpha\beta} = \frac{1}{2}\left(h_{\alpha}{}^{\mu}{}_{,\beta} + h_{\beta}{}^{\mu}{}_{,\alpha} - h_{\alpha\beta}{}^{,\mu}\right) \tag{1.3.2}$$

$$R_{\mu\nu} = \frac{1}{2}\left(h_{\mu}{}^{\alpha}{}_{,\nu\alpha} + h_{\nu}{}^{\alpha}{}_{,\mu\alpha} - h_{\mu\nu,\alpha}{}^{\alpha} - h_{,\mu\nu}\right) \tag{1.3.3}$$

As a result of Equations (1.3.2) and (1.3.3), and defining $\bar{h}_{\mu\nu} = h_{\mu\nu} - \frac{1}{2}\eta_{\mu\nu}h$, Einstein's field equations, $G_{\mu\nu} = 8\pi T_{\mu\nu}$ where $T_{\mu\nu}$ is the stress-energy tensor, become Equation (1.3.4). By applying the tensor analogy of the Lorentz gauge, $A_{\alpha},^{\alpha} = 0$, which is $\bar{h}^{\mu\alpha}{}_{,\alpha} = 0$, Equation (1.3.4) becomes Equation 1.3.5.

$$-\bar{h}_{\mu}{}^{\alpha}{}_{,\nu\alpha} - \eta\bar{h}_{\alpha\beta},^{\alpha\beta} + \bar{h}_{\mu\alpha},^{\alpha}{}_{\nu} + \bar{h}_{\nu\alpha},^{\alpha}{}_{\mu} = 16\pi T_{\mu\nu} \tag{1.3.4}$$

$$-\bar{h}_{\mu\nu,\alpha}{}^{\alpha} = 16\pi T_{\mu\nu} \tag{1.3.5}$$

By comparing Equation (1.3.5) and the metric, $g_{\mu\nu} = n_{\mu\nu} + \bar{h}_{\mu\nu}$ to the equation of electromagnetism, $A^{\alpha}{}_{,\alpha}$ and $-A^{\mu}{}_{,\alpha}^{,\alpha} = 4\pi J^{\mu}$, one can see the difference is only in the addition of an extra index, ν. Therefore since it is known that electromagnetic plane waves are a solution to the electromagnetic equa-

tions, gravitational plane waves are a solution to the gravitational equations, Equation (1.3.6).

$$\begin{aligned} \bar{h}^{xx} &= \bar{h}^{xx}(t-z) \\ \bar{h}^{xy} &= \bar{h}^{xy}(t-z) \\ \bar{h}^{yy} &= \bar{h}^{yy}(t-z) \\ \bar{h}^{\mu z} &= 0 \text{ for all } \mu, \\ \bar{h}^{\mu 0} &= 0 \text{ for all } \mu. \end{aligned} \tag{1.3.6}$$

The simplest way to show that asymmetric motion produces gravitational waves in the linearized case leads to the quadrupole expression for the emitted waveforms. This method shows that unlike electromagnetic waves, gravitational waves are quadrupolar waves. The dominant term in the radiation depends on the varying quadrupole of the source. In contrast, electromagnetic radiation dominantly arises from a varying dipole moment. The dominant term in the gravitational radiation is given by $L_{gravitational-quadrupole} = \frac{1}{5}\left\langle \dddot{\vec{\mathcal{I}}}^2 \right\rangle = \frac{1}{5}\left\langle \dddot{\mathcal{I}}_{jk}\dddot{\mathcal{I}}_{jk} \right\rangle$, where the one-fifth comes from the tensor calculations, $\langle \cdots \rangle$ means to average over several characteristic periods, and $\mathcal{I}$ is given by Equation (1.3.7) where m_i are the component masses and ρ is the mass density.

$$\mathcal{I}_{jk} = \Sigma_i m_i \left(x_{ij} - \frac{1}{3}\delta_{jk} r_i^2 \right) = \int \rho \left(x_{ij} - \frac{1}{3}\delta_{jk} r_i^2 \right) d^3x \tag{1.3.7}$$

By looking at the luminosity from a gravitational wave, one can infer

that it depends on the moving mass (M), the size of the system (R), and the time it takes the mass to move (T) so that $\dddot{I}_{jk} \sim \frac{MR^2}{T^3} = \frac{M(R/T)^2}{T}$. The second equation describes the non spherical part of the kinetic energy divided by the time of movement ("non-spherical" because the motion must be asymmetric.). The result is that $\dddot{I}_{jk} \sim L_{internal}$ where $L_{internal}$ is the power flowing from one side of the system to the other; together with the equation for the gravitational-quarupole, this means that the power output, luminosity, of the gravitational wave is roughly the same as the square of the internal power.

Additionally looking at the equation for the power contained in a gravitational wave, its luminosity, one can see that the less time it takes for particles to move the more power is emitted. If there are two point like particles inspiraling towards each other, when they are closer and moving faster due to conservation of angular momentum the wave emitted from the system will contain more power. Therfore as two bodies like binary black holes fall into one another, the late inspiral and merger will contain more power than the earlier waveform making it important to include this portion of the wave in data filters, templates, when the merger is in the detector's frequency sensitivity range.

The quadrupolar formulation also describes the orbital period of a compact binary system like a binary black hole system. The luminosity of the gravitational wave is roughly the square of the circulating power which is roughly the angular frequency times the potential energy of the system. According to Kepler's laws for two stars of mass m_1 and m_2 the angular frequency ω

is related to the separation of the stars, r, by $\omega^2 r^3 = m_1 + m_2 = M$. The kinetic energy is given as $KE = -\frac{1}{2}PE = \frac{1}{2}\frac{m_1 m_2}{r}$. Therefore, the power of the gravitational wave is given by Equation (1.3.8) substituting $\mu = \frac{m_1 m_2}{M}$. When the calculation is done from $L_{GW} = \frac{1}{5}\left\langle \dddot{I}_{jk} \dddot{I}_{jk} \right\rangle$, one obtains Equation (1.3.9).

$$L_{GW} \sim \omega^2 (KE)^2 = \left(\frac{M}{r^3}\right)\left(\frac{m_1 m_2}{r}\right)^2 = \frac{\mu^2 M^3}{r^5} \tag{1.3.8}$$

$$L_{GW} = \frac{32}{5}\frac{\mu^2 M^3}{r^5} \tag{1.3.9}$$

$$\frac{dE}{dt} = \frac{1}{2}\left(\mu M / r^2\right)\frac{dr}{dt} = -L_{GW} = -\frac{32}{5}\frac{\mu^2 M^3}{r^5} \tag{1.3.10}$$

Integrating Equation (1.3.10) from an initial orbital radius r_o to the some radius , r, and from some initial time, $t = 0$, to the some time, t, the radial distance between the two bodies as a function of time becomes Equation (1.3.11), where $\tau_0 = \frac{5}{256}\frac{r_o^4}{\mu M^2}$. τ_0 is the chirp time of the system, the amount of time needed for the two bodies to come to a radial separation of zero.

$$r^4 = r_o^4\left(1 - \frac{t}{\tau_0}\right) \tag{1.3.11}$$

Using Kepler's law, $T^2 = \frac{4\pi^2}{M} r^3$ where T is the period, the period of the orbit can be determined, Equation (1.3.12), where $m_c = \mu^{\frac{3}{5}} M^{\frac{2}{5}}$. m_c is known as the chirp mass and is often used to describe the mass of the binary instead of the component masses.

$$
\begin{aligned}
T^2 = &\quad \tfrac{4\pi^2}{M} r_o^3 \left(1 - \tfrac{t}{\tau_0}\right)^{\frac{3}{4}} \\
T = &\quad 2\pi \left(\tfrac{256}{5}\right)^{\frac{3}{8}} \mu^{\frac{3}{8}} M^{\frac{1}{4}} \left(\tau_0 - t\right)^{\frac{3}{8}} \\
T = &\quad 2\pi \left(\tfrac{256}{5}\right)^{\frac{3}{8}} m_c \left(\tfrac{\tau_0 - t}{m_c}\right)^{\frac{3}{8}}
\end{aligned}
\tag{1.3.12}
$$

1.4 An Overview of Gravitational Wave Astronomy With LIGO

The LIGO laboratory consists of two observatories located at two sites in the United States: Hanford, Washington and Livingston Parish, Louisiana. Both sites house interferometers with 4 km long arms, *H1* and *L1* respectively. Through June 2009 as part of the Initial LIGO design, the Washington site also housed a second interferometer with 2km long arms in the same vacuum tube as the 4km instrument, *H2*.

A first round of upgrades to LIGO was completed in July of 2009 before the latest data was collected, called S6. In the upgraded state the detectors were called Enhanced LIGO. Currently both LIGO sites are undergoing a second round of upgrades to increase their sensitivity range after which the detectors will be called Advanced LIGO. The upgrades are expected to produce a ten fold increase in the detection range for neutron star binaries to a distance of 200Mpc. Until the Advanced LIGO upgrades are completed, neither LIGO site is operation. *Virgo* is a European based collaboration with a 3km interferometer located in Pisa, Italy, *V1*. This section describes the basics of the initial LIGO detectors. More information is available in [8].

Gravitational waves (GWs) have a transverse quadrupolar nature, so differential changes in the arm lengths of a Michelson interferometer are well matched to detect and characterize the wave. Initial LIGO was designed to be sensitive to GWs in the frequency band $40-700$Hz and was capable of detecting wave strains in amplitude as small as 10^{-21}. Figure 1.1 shows LIGO's best sensitivity curves through the S5 science run.

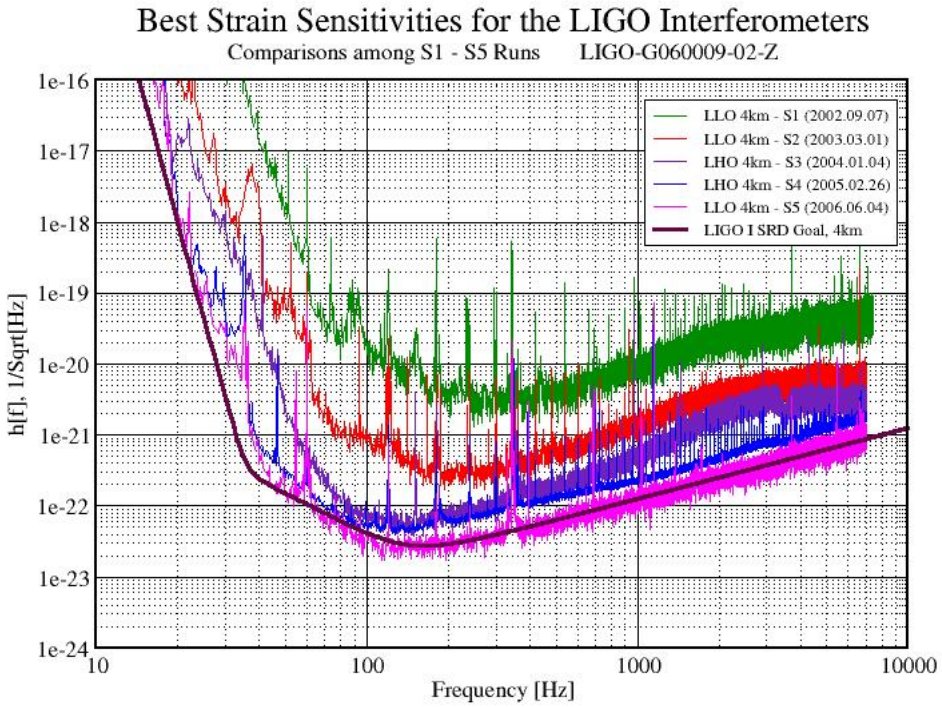

Figure 1.1: LIGO's best strain sensitivities for the first five science runs, [56].

From November 2005 to September 2007, the LIGO detectors operated

at design sensitivity in a continuous data-taking mode. This period represents LIGO's fifth science run and is known as *S5*. Beginning in May 2007, the Virgo detector conducted its second science run and the time period when all three detectors were operational is referred to as *S5VSR2*. From July 2009 to October 2010, the LIGO detectors collected the data known as *S6*.

A Michelson interferometer consists of two arms of equal length joined at one end. At the apex is a beam splitter and at the end of each arm a mirror, end test mass (ETM), is placed. A laser beam, for LIGO a diode-pumped, Nd:YAG laser emitting 10W in a single frequency at 1064nm [8], is shot towards the the beam splitter. The splitter is aligned so that the beam is separated equally into the two arms, reflected off the ETM, recombined at the splitter and transmitted backwards to the laser, called the symmetric port, and no light is transmitted out the fourth side of the beam splitter, the asymmetric port (AS), see Figure 1.2. If a gravitational wave passes through the interferometer, light will exit the asymmetric port and be detected by a photo-diode.

The basic design of a Michelson interferometer is modified in LIGO and Virgo with Fabry-Perot cavities and power recycling mirrors. A Fabry-Perot cavity increases the sensitivity of an interferometer by effectively increasing the arm length. Interferometer sensitivity is directly proportional to the arm length. The design is simple, partially reflecting mirrors are placed closed to the beam splitter between it and the ETMs. The partially reflecting mirrors become the inner test masses (ITMs) in each arm. The ITMs are coated to

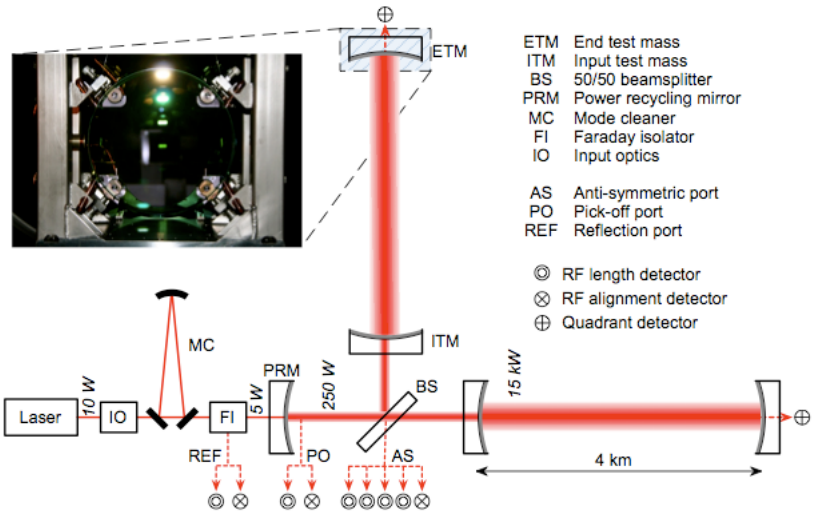

Figure 1.2: The general layout of a LIGO interferometer (the laser power numbers here are generic; specific power levels are given in Table 1 of [8]).

allow light from the beam splitter to pass through but to only allow a small amount of the light reflected from the ETMs to pass back to the laser source thus forcing the light to bounce back and forth between the ITMs and the ETMs traveling further than it would in a simple interferometer.

A second LIGO modification of a Michelson interferometer is a *power recycling mirror*, PRM. This is another partially reflecting mirror which is placed between the laser source and the beam splitter. The result is an effective increase in the power of the laser and in the sensitivity of the detector. For more information on the specifications of the LIGO detectors see [8].

Chapter 2

Gravitational Wave Modeling

The most efficient way to detect gravitational waves from sources like the ultimate inspiral of PSR 1913+16, or the inspiral, merger and ringdown of other binary systems like black hole neutron star binaries or black hole binaries, is to carry out an optimally filtered search. Such a search correlates the detector data stream against analytically described waveforms; thus the shape of the expected waveform needs to be known. The filters used in LIGO and Virgo CBC searches are referred to as *templates* and cover a wide parameter range.

This dissertation discusses the viability of using phenomenological templates, which analytically model hybridized waveforms, see section 2.3, having component spins either aligned or anti-aligned with the total angular momentum of the system. Therefore, this chapter presents several techniques for determining the shape of a wave produced from a given pair of merging, compact objects. Firstly I discuss the post-Newtonian (PN) formalism which is valid in the weak field region, generally taken to be up to the last several cycles

of the inspiral known as the plunge where the orbits can no longer be treated as adiabatically shrinking circles. Secondly I discuss numerical techniques for the strong field region, the plunge, merger, final coalescence and ringdown of the masses. Finally I address hybridization techniques which combine PN and numerical results and give an example of a phenomenological waveform. Such combination waveforms are the basis of the family of templates used in 35-100$M_{\odot}$ mass range known within the LIGO CBC group as the *highmass range*.

2.1 An Overview of Post Newtonian Formalisms

The post-Newtonian (PN) formalism allows for the calculation of the inspiral part of the gravitational wave. Figure 2.1 illustrates the location of the different stages of the waveform with respect to one another. Some PN formalisms like the effective-one-body method, EOB, allow computation of the waveform up to the transition to the merger, [1, 3, 67]. In general, comparison with accurate numerical results is the only way to determine the appropriate region of validity of the PN waveforms.

PN formulations are valid when the gravitational field is weak enough for Newtonian gravity to be a correct approximation to the gravitational field. The Newtonian description then provides the lowest order in potential strength: the Newtonian limit, $\epsilon^2 = \phi \sim v^2/c^2$, where v is a function of time corresponding to the orbital velocity of the system. General relativistic effects then appear as small higher order corrections to the field and are de-

rived from a Taylor series expansion in powers of ϵ. The PN order is defined to be half the power of ϵ adjusted so that ϵ^0 is the Newtonian limit and ϵ^2 is the first order PN term denoted 1PN. The effects of gravitational radiation are not apparent until the 2.5PN term. Therefore to use the PN approximation in modeling gravitational waves at least the 2.5PN term must be calculated. The PN formalisms have been used to describe the precession of the perihelion of Mercury [23], the equations of motion for binary pulsars [9, 18, 25, 36], solar-system tests of general relativity [82–85], and gravitational radiation reaction [13, 16].

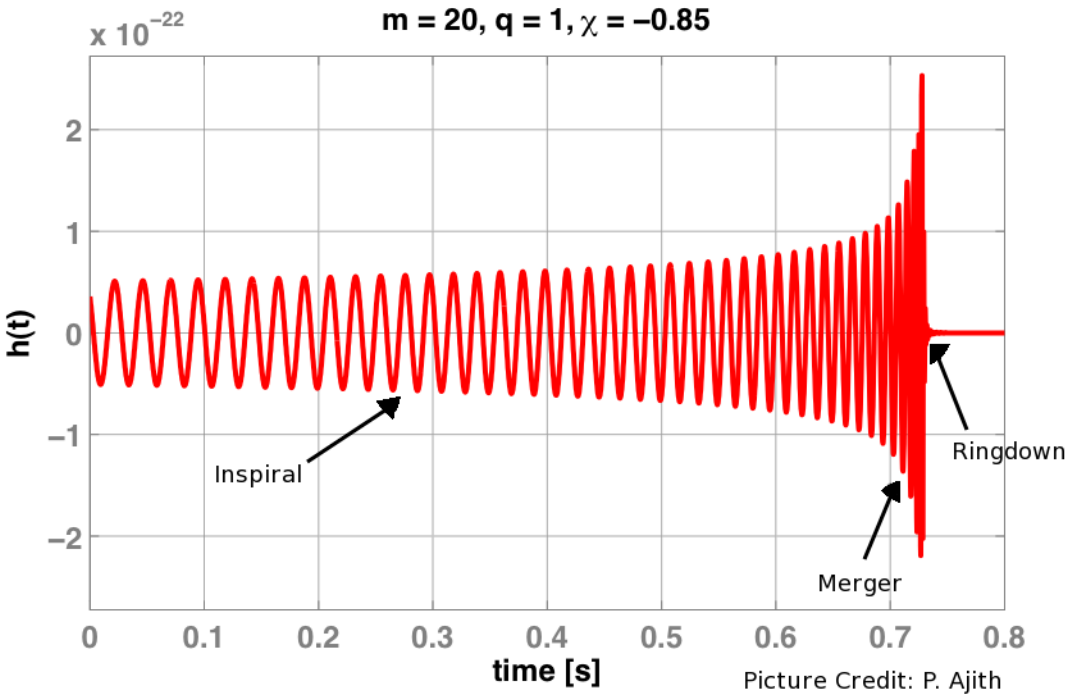

Figure 2.1: A spinning IMRSA waveform with: total mass $20M_\odot$, $q = m_1/m_2 = 1$ and $\chi = -0.85$, illustrating the different stages of the waveform: inspiral, merger, and ringdown.

The PN description of inspirals is used by LIGO in the creation of *templates*, data filters that model potential signals. For signals like binary neutron stars or binary black hole neutron star pairs with total masses between 1 and $35M_{\odot}$, PN inspirals are used as templates, [59]. In general, only the phase of the waveform is approximated in this method. The amplitude is set to mass-quadropole order. Waveforms approximated in this way are referred to as *restricted PN waveforms*. For highmass systems, a complete waveform spanning from inspiral to ringdown is required and restricted PN waveforms or EOB waveforms are used in conjunction with numerically computed waveforms, see Section 2.2.

2.2 Basic Numerical Relativity Techniques

PN expansions work for the early stages of the inspiral; however for the plunge, the merger, and the ringdown, other methods are needed. Current computational approaches, known as numerical relativity, can now model all the stages of a binary black hole merger, by solving the full non-linear Einstein equations. These computations require large computer resources where the necessary memory resources and the amount of time needed to calculate the waveforms are heavily dependent on the details of the system and are near current computational limits, making it impractical to complete a template based analysis purely with numerically generated templates.

The underlying concept behind numerical relativity is to start with a

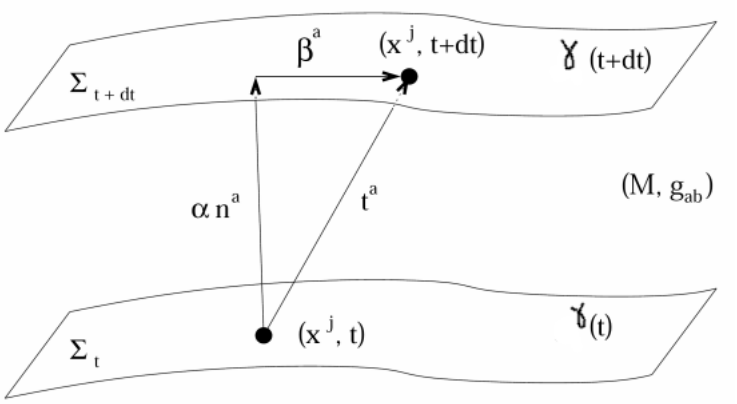

Figure 2.2: An illustration of the relation between time slices in the ADM formalism. n_a is a unit time like normal to the slice. t_a is the direction of flow of the time coordinate in the chosen coordinate system. Image is from [45]

metric form similar to

$$ds^2 = -\alpha dt^2 + \gamma_{ij}\left(\beta^i dt + dx^i\right)\left(\beta^j dt + dx^j\right)$$

which is the $3+1$ Arnowitt, Deser and Misner (ADM) decomposition of the metric into time and space using the lapse α, shift β^i and spatial metric γ_{ij}. The metric describes how the system develops in 4-space given the coordinate choice α, β^i, and a set of initial data from which to iteratively evolve the system. In the metric, α controls the size of the proper time step taken between the 3-spaces of constant coordinate time, Σ_t; β^i describes how the spatial locations map between coordinate time surfaces, Σ_t. γ_{ij} is the metric of the 3-space Σ_t. Consistency equations assure that the $\{\Sigma_t\}$ are correctly embedded in the 4-space. See Figure 2.2.

The system is evolved from a set of initial conditions consisting of a 3-space field for γ_{ab} and another for its momentum K_{ab} describing the system of interest at an arbitrarily chosen time, "$t = 0$". The initial conditions must satisfy a set of four elliptical equations at $t = 0$; these are the consistency equations. The remaining six Einstein equations are the evolution equations. One can evolve forward in time with any preferred computational method, which discretizes both derivatives in space and time. In particular, the initial conditions are evolved in order to obtain the system at Δt; then that answer is used to evolve to obtain the system at $2\Delta t$. The process is repeated as many times are needed to fully progress the system. In practice a more elaborate scheme making use of a careful choice of computational methods is needed to maintain *numerical* stability.

Numerical results are too computationally expensive to produce the large number of long waveforms needed for GW search templates, and those produced quickly often contain too few cycles. However, numerical waveforms can be extended with PN formalisms to create hybrid waveforms, an intermediary step towards the phenomenological waveforms usable by LIGO CBC searches.

2.3 Hybrid Techniques

Numerical simulations have been able to model the entirety of a gravitational wave. However they are computationally very inefficient at modeling the long pre-merger inspiral needed for LIGO templates. Due to this large computa-

tional demand, it is not feasible for numerical relativity to create templates containing all three stages, inspiral, merger, ringdown, of the gravitational wave. Computational results *are* used in a hybrid technique where inspirals and ringdowns calculated through perturbative methods like PN are "stitched" onto numerically generated mergers to create a complete waveform. The following subsections give an overview of a few template *families* whose analytical models are constructed by fitting such hybrid waveforms.

2.3.1 Inspiral Merger and Ringdown Waveforms

The term inspiral, merger and ringdown (IMR) waveform is used both for a class of templates and to refer to any waveform that contains all three stages of evolution. In LIGO, IMR templates are nonspinning phenomenological templates analytically describing hybrid waveforms generated by matching numerical-relativity waveforms containing the plunge, merger and ringdown to TaylorT1 approximants in the frequency domain. The Taylor T1 approximants produce 2.5 restricted PN waveforms [68]. The computational black hole horizon masses, m_1 and m_2, are matched to a PN system with the same mass parameters. It is assumed that the phase does not change form during the waveform; therefore, the phase during the whole waveform is given by the same equation as during the inspiral stage, [65]. The amplitude is approximated with a fitting function during the plunge and a Lorentzian function chosen so that the amplitude is continuous during the transition from the plunge to the merger, see Section 2.3.2. The ringdown is modeled by fitting to numerical

relativity simulations.

Other types of IMR waveforms use different PN formalisms. One IMR waveform, EOBNR (effective one body numerical relativity), uses the EOB (effective one body) formalism, [4,60,67,87] to model the inspiral and plunge. EOB inspirals are tuned to numerical waveforms in a process described in [40]. EOB hybrids use the same hybridization techniques as the IMR waveforms. However, the EOB formalism models the late inspiral and plunge more accurately, so is in principle better for highmass sources, those from $35 - 100 M_{\odot}$, for which these parts of the waveforms are in the LIGO sensitivity range. Therefore, EOB hybrids were analytically modeled to create EOBNR templates that were used in the S5 highmass search, [40]. However they only model nonspinning sources. Other families have been and are being developed for the highmass region to handle spinning sources. This dissertation evaluates one particular family called IMR Spin Aligned (IMRSA) templates. The details of this family are discussed in the next section.

As stated above, the IMR waveforms and the EOBNR waveforms used by highmass LIGO CBC searches model only non-spinning systems. So while they represented a step forward in the highmass regime, they do not fully model the systems that may inhabit that region.

Spinning systems fall into one of two categories: precessing and non-precessing. Precession of the orbital plane occurs when the spins of the component masses are not (anti-)parallel with the orbital angular momentum, $\vec{L}$, of the system. In such systems, each of the angular momenta, $\vec{S}_i$, $\vec{L}$, precesses

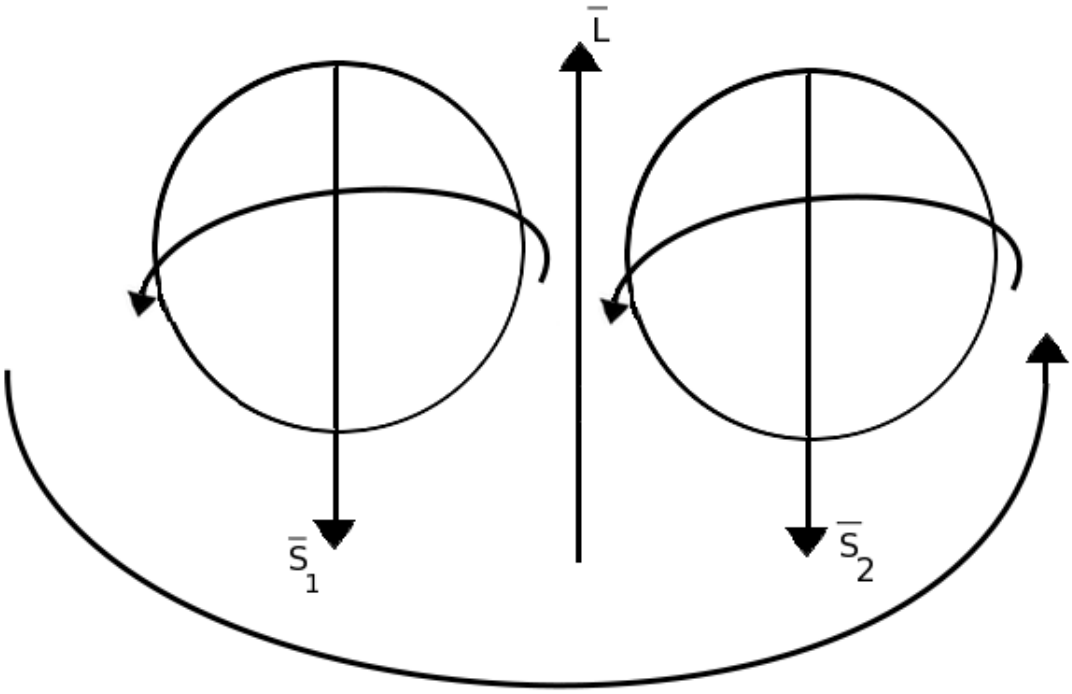

Figure 2.3: A cartoon showing the relation between conponent spins, $\vec{S_i}$, and orbital spin, $\vec{L}$, in the anti-aligned case.

around the total angular momentum, $\vec{J}$. In particular, since the orbital plane is perpendicular to $\vec{L}$, it precesses. Figure 2.3 shows an anti-aligned case. In non precessing systems, the orbital plane is stationary and the component spins are aligned or anti-aligned with the orbital momentum.

Precessing systems are very complex due to the number of parameters needed, 12 compared to the 3 for spin aligned or anti-aligned sources and two for non-spinning sources, to model the individual spins. Precessing waveforms reflect that complexity and show modulation at the various pre-

cession frequencies atop the inspiral waveform. Creating analytical models of precessing waveforms is not a simple task, but waveforms of non-precessing waveforms have been developed. These nonprecessing waveforms, called *IMR Spin Aligned* (IMRSA) waveforms, are a first attempt to model spin in the highmass range and are discussed in Section 2.3.2.

2.3.2 Inspiral Merger and Ringdown Spin Aligned Waveforms

This dissertation centers around the evaluation of IMRSA waveforms as LIGO CBC search templates. Specifically it analyzes a family called IMRPhenomB described in [65]. Another family that needs investigation is the family described in [58] which has yet to be named. This section describes the formulas used to generate IMRPhenomB templates, which from here on are called IMRSA templates.

IMRSA templates are phenomenological waveforms modeling the dominant angular harmonic of gravitational radiation from BBHs with non-processing spins: spins that are aligned or anti-aligned with the orbital angular momentum [65]. Phenomenological waveforms are analytical models of hybrid waveforms where some coefficients are determined through a tuning process. Hybrid waveforms are made from a combination of post-Newtonian waveforms for the inspiral, fit to numerical relativity results for the merger and early ringdown phases [65], and to perturbation theory for the late ringdown. Aligned binaries, specifically those where all the angular momentum vectors are aligned

with each other, are expected to form from isolated binary evolution relevant to LIGO in gas-rich galactic clusters. Additionally supermassive black hole mergers are expected to produce aligned spin signals relevant to the proposed space based detector LISA [72, 77, 80].

When the spin of a black hole is not zero, three additional parameters are needed to describe it: a spin parameter for each spatial direction. For spinning binary black holes, spin introduces a total of six parameters. However when the component spins are restricted to be either aligned or anti-aligned with the total angular momentum, the leading spin-orbit term in the PN expansion is dominated by called χ, the combined spin defined in Equation (2.3.1). Each template can be described by a set of parameters: M, η and χ defined by (2.3.1), [65]. The PN analytical waveforms are constructed in the Fourier domain as described in [65] and are given in Equation 2.3.2 below.

$$\begin{aligned} M &= m_1 + m_2 \\ \eta &= m_1 m_2 / \left(m_1 + m_2\right)^2 \\ \delta &= \left(m_1 - m_2\right) / \left(m_1 + m_2\right) \\ \chi_i &= S_i / m_i^2 \\ \chi &= \tfrac{1+\delta}{2}\chi_1 + \tfrac{1-\delta}{2}\chi_2 \end{aligned} \tag{2.3.1}$$

$$
\begin{aligned}
h\left(f\right) &\equiv A\left(f\right)e^{-i\Psi(f)} \\
A\left(f\right) &\equiv Cf_1^{-7/6}\left\{\begin{array}{ll} f'^{-7/6}\left(1+\sum_{i=2}^{3}\alpha_i\nu^i\right) & f<f_1, \\ w_m f'^{-2/3}\left(1+\sum_{i=1}^{2}\varepsilon_i\nu^i\right) & f_1\leq f<f_2, \\ w_r\mathcal{L}\left(f,f_2,\sigma\right) & f_2\leq f<f_3, \end{array}\right\} \\
\Psi\left(f\right) &\equiv 2\pi f t_0+\varphi_0+\tfrac{3}{128\eta\nu^5}\left(1+\sum_{k=2}^{7}\nu^k\Psi_k\right)
\end{aligned}
\tag{2.3.2}
$$

In Equation (2.3.2), $h\left(f\right)$ represents the gravitational wave strain, $A\left(f\right)$ is the amplitude of waveform; $\Psi\left(f\right)$ is the phase of the gravitational wave, and f is the Fourier frequency, [65]. Additionally $f'=f/f_1$, $\nu^j\equiv\left(\pi Mf\right)^{(j/3)}$, $\varepsilon_1=1.4547\chi-1.8897$, $\varepsilon_2=-1.8153\chi+1.6557$; C is a numerical constant whose value depends on the sky-location, orientation and the masses of the system; and $\alpha_2=-323/224+451\nu/168$ and $\alpha_3=\left(27/8-11\nu/6\right)\chi$ are the PN corrections to the Fourier domain amplitude of the $(l=2,m=\pm2)$ mode PN inspiral waveform; t_0 is the time of arrival of the signal at the detector; and φ_0 is the corresponding phase, $\mathcal{L}\left(f,f_2,\sigma\right)$ is a Lorentzian function with width σ centered around the frequency f_2; w_m and w_r are normalization constants chosen so as to make $A\left(f\right)$ continuous across the "transition" frequencies f_2 and f_1; and f_3 is a convenient cutoff frequency such that the power of the signal above this frequency is negligible, [65]. The phenomenological parameters Ψ_k and $\mu_k\equiv\left(f_1-f_{LSO}^0,f_2-f_{QNM}^0,\sigma-f_{QNM}^0/Q^0,f_3\right)$ are written in terms of the physical parameters of the binary as: $\Psi_k=\sum_{i=1}^{3}\sum_{j=0}^{N}x_k^{(ij)}\eta^i\chi^j$, $\mu_k=\sum_{i=1}^{3}\sum_{j=0}^{N}\frac{y_k^{(ij)}\eta^i\chi^1}{\pi M}$, where $N\equiv\min(3-i,2)$ while $x_k^{(ij)}$ and $y_k^{(ij)}$ are tabulated

in [65], and the values of ψ_k and μ_k are estimates from the hybrid waveforms [65]. When $\eta \to 0$ the phenomenological parameters become:

$$f_1 \to f^0_{LSO}, f_2 \to f^0_{QNM}, \sigma \to f^0_{QNM}/Q^0, \Psi_k \to \Psi^0_k$$

f^0_{LSO} and f^0_{QNM} are the last stable orbit [42] and the dominant quasi-normal mode [27], and Q^0 is the ringdown quality factor of a Kerr black hole with mass M and spin χ ($Q^0 = \omega_s \tau_s$ where ω_s is the ringdown's frequency and τ_s is the ringdowns's damping time) ranging from $2 \to \infty$, while Ψ^0_k are the (2PN) Fourier domain phasing coefficients of a test-particle inspiraling into the Kerr black hole, computed using the stationary-phase approximation, [27, 49].

The difference between a spin aligned template and a spin anti-aligned template is demonstrated in Figure 2.3.2, which shows only the late inspiral, merger and ringdown of the templates. The two waveforms are generated so that the initial frequency is $20Hz$; with this condition, the spin aligned template is longer than the spin anti-aligned template. Also the spin aligned template has a higher frequency before the plunge, $1028.179Hz$ compared the anti-aligned templates frequency of $848.140Hz$.

The IMRSA templates are an analytical model of hybrid waveforms made from PN inspirals and numerical results for the merger and ringdown; such models are called phenomenological templates. IMRSA templates are a first step towards being able to handle more complicated systems like precessing waveforms. In this dissertation however only non-precessing spin waveforms will be considered; from here on *spinning* will be understood to mean

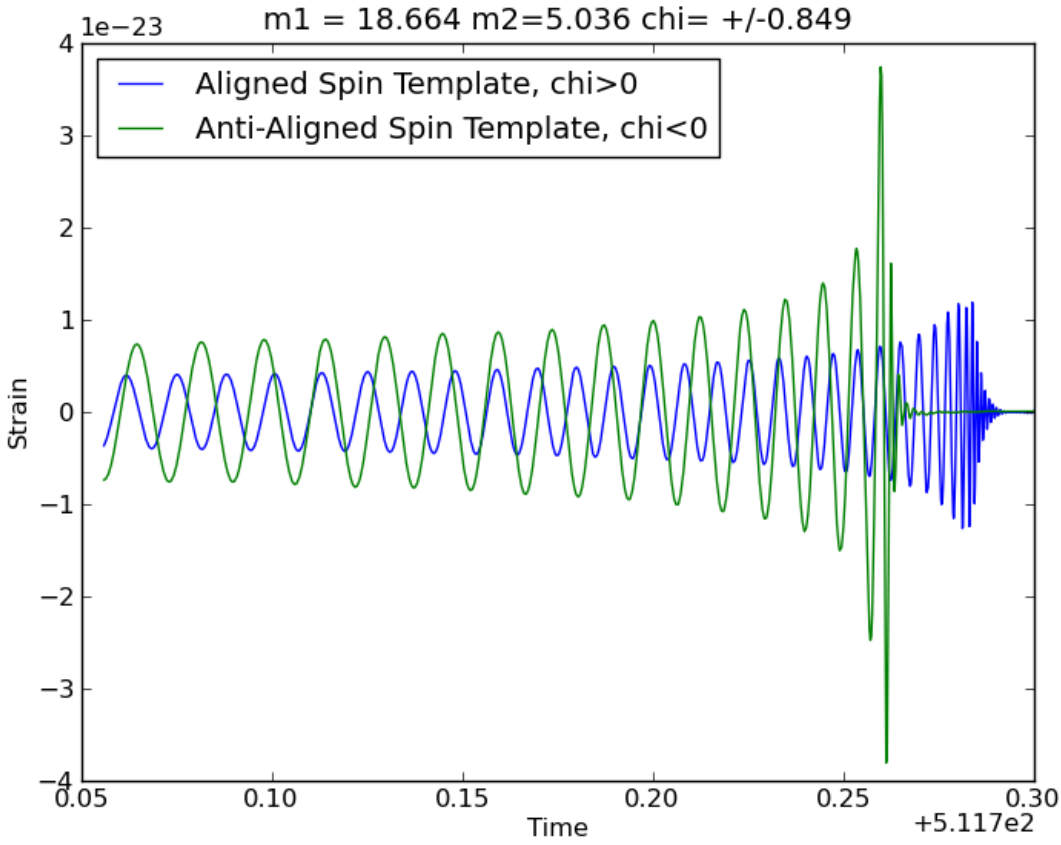
m1 = 18.664 m2=5.036 chi= +/-0.849
1e−23
Aligned Spin Template, chi>0
Anti-Aligned Spin Template, chi<0
Strain
Time
+5.117e2
4
3
2
1
0
−1
−2
−3
−4
0.05
0.10
0.15
0.20
0.25
0.30

non-precessing.

2.4 NINJA2

NINJA2 is a collaboration between LIGO-Virgo data analysts and numerical relativity groups. The collaboration allows for the assessment and tuning of LIGO-Virgo analysis searches for complex sources like numerically simulated waveforms from the plunge, merger and ringdown of compact binary systems. NINJA2 is a valuable tool to systematically study the parameter space of binary black holes. The waveforms it produces enable studies like this one to characterize the efficiency of detection/parameter-estimation of data analysis pipelines employing state-of-the-art NR-PN templates. Ultimately these studies will be performed on fully non-stationary and non-Gaussian data containing the numerical waveforms collected by the collaboration, [71]. The analysis presented in this dissertation has only been performed on the two week colored Gaussian noise data set produced by the collaboration.

The NINJA2 datasets represent a unique data analysis challenge. The collaboration first produced a short data set of two weeks of colored Gaussian noise with hybrid waveforms, and then a longer two month data set with colored Gaussian noise and hybrid waveforms. The noise is colored by the Initial LIGO sensitivity curve for *H1* and *L1*, and by the Virgo sensitivity curve for *V1*. The dataset containing real data has not yet been released to the collaboration. The release of the longer Gaussian noise data corresponded with the writing of this dissertation; therefore, the results shown here are only

for the two weeks of Gaussian noise data previously available. The hybrid waveforms represent non-precessing spinning waveforms with component spins between -0.85 and 0.85, mass ratios $1 \leq m_1/m_2 \leq 10$ and with total masses greater than or equal to $10M_{\odot}$ [71]. The waveforms are made from numerical relativity simulations with at least five orbits before merger and with amplitude error less than five percent, matched to post Newtonian solutions representing the early inspiral [71]. For more information on the actual waveforms injected into each interferometer's dataset, see [35] and [71]. Due to the types of injections made, the NINJA2 datasets are an excellent opportunity to test IMRSA waveforms as LIGO-Virgo templates.

Chapter 3

gstlal

The following section discusses the general structure of a CBC analysis pipeline. It also compares the pipelines used in this analysis, using *lloid* algorithm, with the standard LIGO CBC pipeline *ihope*, using the *FINDCHIRP* algorithm, to motivate the choice of *lloid* over *ihope*. The main difference applicable to this dissertation is that in *lloid* a singular value decomposition of the search templates provides a basis of the template bank, and the basis is used in the matched filter instead of the original templates.

3.1 General Pipeline Structures

The calibrated output of the interferometers is analyzed for gravitational waves by several groups in the LIGO Virgo Collaboration (LVC). The compact binary coalescence working group, called CBC for short, analyzes the data for compact binary systems via a matched filtering engine which is at the heart of the

CBC's analysis pipeline. The general idea of the CBC pipeline is to take the calibrated detector data stream and output databases of *coincident triggers*, possible gravitational wave detections found in multiple interferometers taking into account light travel time between detectors. This is done with some delay (latency) with regards to the initial collection of the data that depends on the particular search. The current pipeline draws code form the *LIGO Scientific Collaboration Algorithm Library* (LAL) to form a pipeline nicknamed *ihope* centered around the *FINDCHIRP* algorithm, [10].

My analysis was performed with a new, unnamed pipeline using the *gstlal* code bank. *gstlal* uses LAL and *gstreamer*. gstreamer is a stream based code available on Linux machines designed for use as a streaming media player. gstreamer is organized around blocks of code called elements, which perform specific tasks [33]. Elements are arranged in specific sequences to execute complex tasks. In the case of gstlal, the elements are arranged in a pipeline and often execute calls to programs and/or functions from LAL. Depending on the type of sources being searched for, different elements are used. The analysis described below represents the first test of a gstlal pipeline from start to finish, specifically the low-latency online inspiral detection, known as *lloid*, which corresponds to *ihope*'s *FINDCHIRP*, [51].

FINDCHIRP meets the demands of Initial and Enhanced LIGO well; however, when advanced detectors come online in 2015, new data analysis challenges are anticipated and it was precisely to meet these needs that *gstlal* and *lloid* were developed. In the advanced detector era, LIGO's frequency sensitiv-

ity bandwidth will increase allowing signals to remain in "band" longer. That means longer templates will be needed to model the longer signals. Working with longer templates is more computationally expensive than working with shorter ones; however, *lloid* was designed to reduce the computational load of these templates. Starting with a waveform template bank, *lloid* creates a basis representing the waveforms in the template bank and orders the basis vectors by their importance in describing the bank. Among its advantages is that careful, even distribution in the signal template bank can be relaxed because the basis determination is fairly insensitive to this placement. An essential ingredient in the method is to invert a non-square matrix; a singular value decomposition is used to do this. Thus the method has acquired the name SVD, see section 3.3.

CBC data analysis pipelines like *ihope* and the ones using *lloid* consist of four main programs. The first fetches the data. The second generates the templates. The third performs the matched filtering. The fourth performs coincidence tests amongst the detectors. The bulk of the analysis takes place in the matched filtering step (for *ihope* this is *FINDCHIRP* and for *gstlal* pipelines is this *lloid*); therefore the discussion here will focus on that step. Schematics of the two pipelines discussed in this dissertation are shown in Figure 3.1, adapted from [19] and Figure 3.2 from [70].

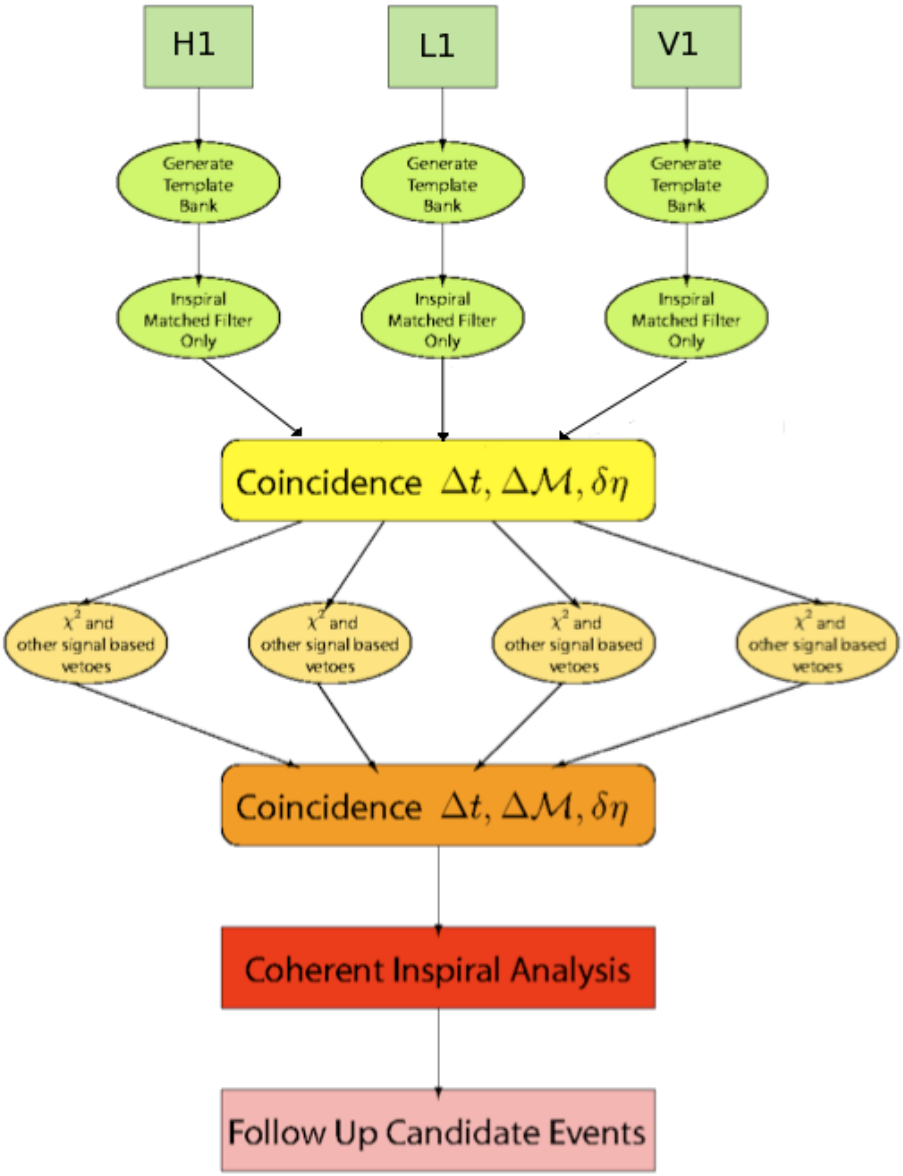

Figure 3.1: A schematic depicting the organization of the ihope search, adapted from [19].

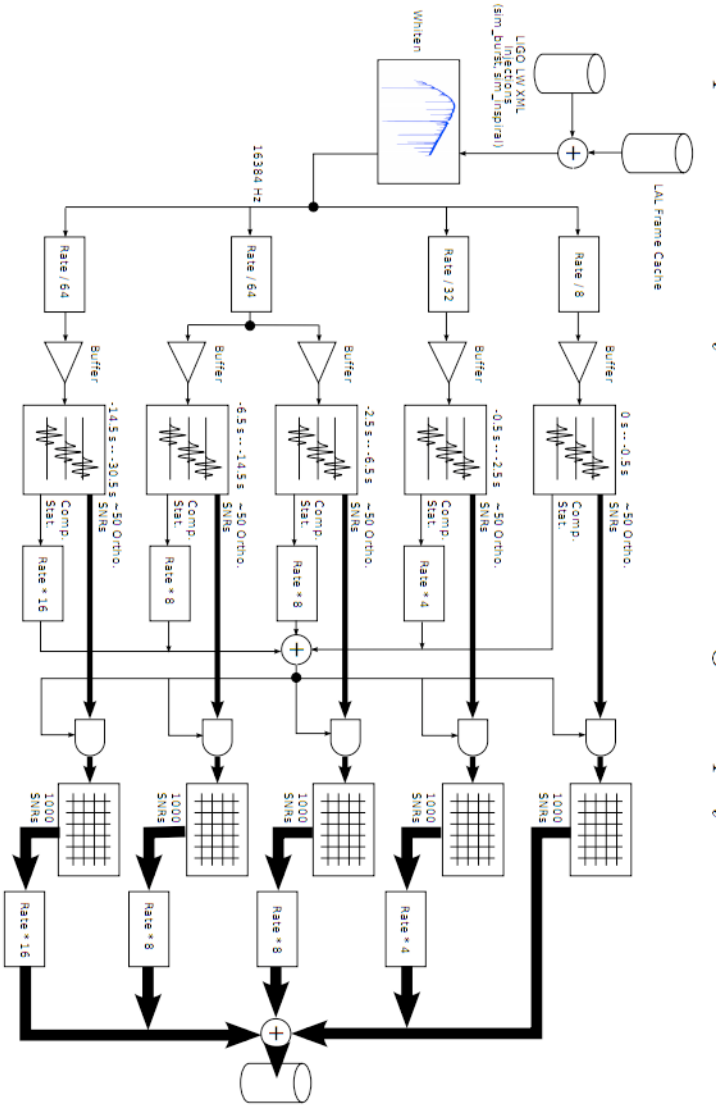

Figure 3.2: A schematic depicting the organization of the lloid search pipeline, [70]. In lloid the data are collected, weighted by a function containing information about the power spectral density of the detector at that time, and then the template banks are generated. The templates are then sliced and resampled so that spectral regions with lower frequency are sampled with fewer points. For each sampling rate, the SVD is calculated, see section 3.3, and the resulting *singular values* are thresholded on at the gate and reassembled into the SNR stream.

3.2 Matched Filtering

Matched filtering is used to determine if a signal is present in the calibrated data stream $s(t)$. When there is no signal, the data is simply a mixture of noise, $n(t)$, stemming from sources as varied as thermal effects and seismic events to trains and helicopters, although many of these events are excised from the data, vetoed, before analysis. When a signal, $h'(t)$, is present in the data time stream, it is often buried in this noise. A matched filter computes the correlation between the resultant cocktail of frequencies in the data to the frequency composition of a possible source. The formula is given in (3.2.1) in which $h(t)$ is the search template, $s(t) = n(t) + h'(t)$ is the signal from the detector and is a combination of the noise in the detector and the waveform if a wave is present; otherwise, it is just the noise. In Equation (3.2.1), $\tilde{h}(f)$ is the Fourier transform of the template, $h(t)$; $\tilde{s}(f)$ is the Fourier transform of $s(t)$; * denotes the complex conjugate, and f is the frequency. C is any constant resulting from the derivation of the filter, see [19]. $S_n(|f|)$ is a function representing the power in a given frequency bin within the data stream and whitens the data.

$$Z(t) = C \int_{-\infty}^{+\infty} \frac{\tilde{s}(f)\,\tilde{h}^*(f)\,e^{2\pi i f t}}{S_n(|f|)} df \tag{3.2.1}$$

The results of the matched filter calculations are used to determine the signal-to-noise ratio, SNR, ρ. The SNR is used to determine if a signal is indeed

present or not in the data. The SNR is the absolute value of $Z(t)$ weighted by its variance σ given by Equation (3.2.2). ρ is given by equation (3.2.3). To determine if a signal is present ρ is thresholded, so that if it is above 5.5 at a specific time a possible detection, trigger, is recorded at that time; otherwise, the data stream at that time is treated as noise and ignored. The value of 5.5 is chosen because it produces a reasonable per detector threshold to expect a few events in background for triple coincidence between the different detectors. For the dataset used in this dissertation, 5.5 is a value several sigma above the Gaussian background so that any trigger above it is known not to be noise.

$$\sigma^2 = 2\int_{-\infty}^{+\infty} \frac{\tilde{h}(f)\,\tilde{h}^*(f)}{S_n(|f|)} df \tag{3.2.2}$$

$$\rho = \frac{|Z(t)|}{\sigma} \tag{3.2.3}$$

3.3 Singular Value Decomposition and *gstlal*

As part of the matched filtering step and before calculating Equation (3.2.1), *gstlal* makes use of a singular value decomposition (SVD) to create a factorization of a matrix constructed from the time series waveforms defined by a template bank. It is similar to an eigenvalue problem except that the input matrix is rectangular rather than square. The input matrix is used to find an

orthogonal basis from which the matrix can be reconstructed, [50]. The SVD produces a list of singular values similar to eigenvalues and corresponding to orthogonal basis vectors similar to eigenvectors. Selecting only the largest singular values results in a smaller, approximate version of the original matrix. The SVD method thus decreases the number of dimensions needed to represent the original matrix by identifying and retaining only these dimensions that have the most effect on the original matrix.

In application to matched filtering, the matrix being decomposed is constructed so that there are two rows for each template, one for the real part and one for the imaginary part of the time series of the template. Therefore if there are N templates in the bank, there will be $2N$ rows in the matrix which is less than the number of sample points in each waveform; thus this is a rectangular matrix, see Equation (3.3.1) where $N >> A$. The SVD method is a way of producing effective inverses of such matrices by generating a list of *singular values* and their associated orthogonal basis vectors. The method in *lloid* is to keep only "enough" of the basis vectors and their associated singular values to effectively cover the template space. The basis vectors are orthogonal, so the response of any template in the bank can be approximately constructed via its weighted correlations between basis vectors and the data. This reduces the number of correlations needed to search a given template bank by an order of magnitude, [50]. Thereby making *lloid* faster than *FINDCHIRP*.

$$[h_A] = \begin{bmatrix} Re\left(h_1\left(t_1\right)\right), & Re\left(h_1\left(t_2\right)\right), & \cdots, & Re\left(h_1\left(t_N\right)\right) \\ Re\left(h_2\left(t_1\right)\right), & Re\left(h_2\left(t_2\right)\right), & \cdots, & Re\left(h_2\left(t_N\right)\right) \\ \vdots & \vdots & \vdots & \vdots \\ Re\left(h_A\left(t_1\right)\right), & Re\left(h_A\left(t_2\right)\right), & \cdots, & Re\left(h_A\left(t_N\right)\right) \end{bmatrix} \tag{3.3.1}$$

Chapter 4

IMRSA Template Banks

Template banks are databases containing the parameters for a collection of search templates. The actual templates are generated as needed by the pipeline, ihope or lloid. The parameters are selected to properly cover the parameter space, meaning there is a 97% overlap between nearest neighbor templates in the bank. A placement metric is generally used to determine which parameter combinations will meet that criterion. In the S5 highmass search, EOBNR template banks were created using a hexagonal placement algorithm in the mass space with the same placement metric calculated for stationary phase approximation templates, [6, 12, 17, 40, 75]. The following section describes how I placed the IMRSA templates to create the template banks and how close to meeting the overlap criterion the placement comes.

4.1 The Distribution of Templates Used

The *ad hoc* banks I used are generated by a three step process. First an EOBNR bank is generated. This means that the templates are placed in the mass space using a hexagonal grid as described in [17]. In the reference the grid is constructed in $\tau_0 - \tau_1$ space in practice $\tau_0 - \tau_3$ space is used. The τ_i's are the post-Newtonian contributions to the time for a gravitational wave to evolve from a minimum frequency to infinity, called *chirp times*, and are a convenient way to represent the masses of the binary system. The chirp times are given by (4.1.1) where M is the total mass, $\eta = \frac{m_1 m_2}{M^2}$, and f_L is the lower frequency cutoff used to generate the template, [14, 17]. The grid has been shown to work for stationary phase approximation inspirals but it may not be the optimal spacing for IMRSA templates. The corresponding m_1-m_2 distribution can be seen in the top plot of Figure 4.1.

$$\begin{aligned} \tau_0 &= \tfrac{5}{256}\eta^{-1}M^{-5/3}\left(\pi f_L\right)^{-8/3} \\ \tau_1 &= \tfrac{5}{192}\left(\eta M\right)^{-1}\left(\tfrac{743}{336}+\tfrac{11}{4}\eta\right)\left(\pi f_L\right)^{-2} \\ \tau_3 &= \tfrac{1}{8 f_L \eta}\left(\pi M f_L\right)^{-2/3} \end{aligned} \tag{4.1.1}$$

Next the allowed range of χ values is discretely sampled. The range of χ values – the spin – allowed for a given mass pair depends on the mass ratio of the template, $q = \frac{m_1}{m_2}$, because the set of numerical waveforms used to construct the phenomenological templates cover a specific parameter space: $\chi \in \{-0.85, 0.85\}$ when $q \in \{0, 4\}$ and $\chi \in \{-0.5, 0.75\}$ when $q \in \{4, 10\}$ [65]. The templates used to produce the results shown below sample each q range

into 15 evenly spaced points. Due to the asymmetry of the allowed spins about zero in the higher mass ratio region the sampling produces no zero spin templates in that range. There is no reason to believe that the χ space has been covered properly. It may be over- or under-populated. The population of the χ-q space can be seen in the bottom plot of Figure 4.1.

The third step is to calculate for each template the *final frequency*, the highest frequency contained in the template. In ihope, the final frequency is not stored in the template bank but calculated as needed. In lloid, it is assumed to be stored in the template bank therefore necessitating this step.

4.2 Template Bank Simulations

A template bank is said to optimally cover a region of parameter space when the overlap between a template and its *nearest neighboring template* is 97%. A higher lever of coverage slows down the search by increasing the number of needed calculations. *Overlap* is defined as the percentage of correlation between two templates, see Equation (4.2.1). A *nearest neighbor template* is the template closest to the original one in the possibly curved parameter space. Some template families have known *placement metrics* describing the curvature of their parameter space that is used to place the templates in order to guarantee the correct amount of overlap between nearest neighbors. Since there is no such known metric for IMRSA templates, I present below a measure of the overlap between the templates.

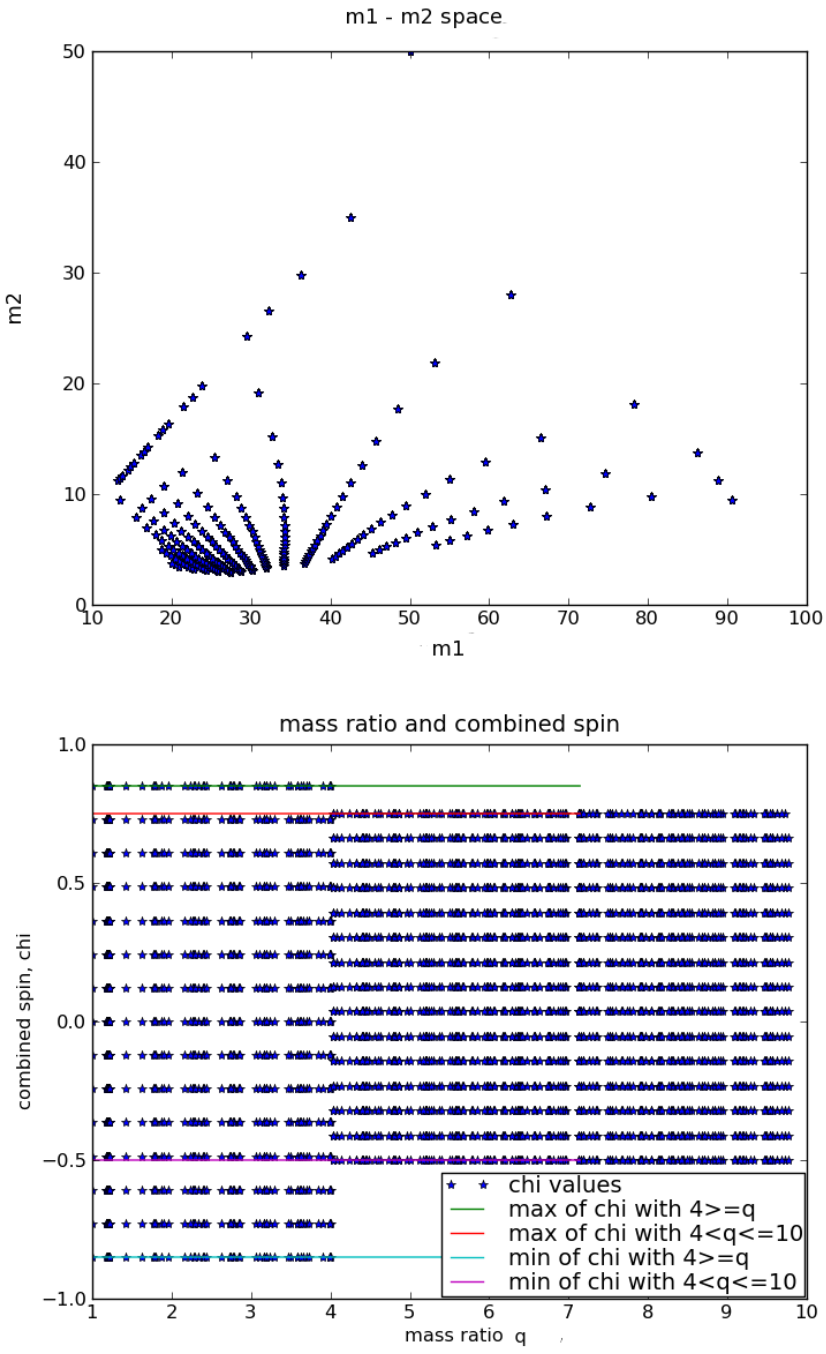

Figure 4.1: The first plot shows the distribution of templates in the m_1-m_2 plane; the second, shows the distribution in the χ-q plane.

$$overlap = \frac{\int \tilde{h}_{1(t)}\tilde{h}_{2(t)}e^{2\pi i f t}}{\int \tilde{h}_{1(t)}\tilde{h}_{1(t)}e^{2\pi i f t}} \times 100\% \tag{4.2.1}$$

The coverage of the bank is measured by use of a tool called template bank simulations, *banksims*. In a banksim, a random template from the parameter space spanned by the bank but that is not itself in the bank is used as an injection and its correlation to every template in the bank is calculated. The correlation is called the *overlap*. Ten banksims were performed on the IMRSA template banks described above in order to determine how well they cover the parameter space. Results from the sixth banksim in Table 4.1 are shown in Figure 4.3. The best overlap was 99.276%. See Table 4.1 for the parameters corresponding to those injections.

The results indicate that the template bank covers the the m_1-m_2 plane well. However in the χ-q plane, the results show the placement to be non-ideal. Some of the issues in the χ-q plane such as the poor q recovery are due to shorter signals like those produced by higher total mass systems. The spread in the χ values is most likely due to the templates not being optimally placed. However, the bank did consistently report the sign of the spin correctly meaning that it was distinguish between spin aligned and spin anti-aligned injections. Also they show that the quality of the bank is improved by the inclusion of spin. Techniques like the use of a stochastic bank, where random templates are used as seeds and the brute force calculations of overlaps between the seed template and potential nearest neighbor templates are done until the bank meets the 97% overlap criterion, may help with the over coverage of the

space, [30,38]. The template banks described above are sufficient for the scope of this dissertation.

Inj Num	Inj m_1 ($M_\odot$) S Temp m_1 ($M_\odot$) NS Temp m_1 ($M_\odot$)	Inj m_2 ($M_\odot$) S Temp m_2 ($M_\odot$) NS Temp m_2 ($M_\odot$)	Inj q S Temp q NS Temp q	Inj χ S Temp χ NS Temp χ	Overlap Spin % NonSpin %
0	35.003	8.995	3.891	-0.801	
	50.980	6.526	7.811	-0.410	94.764
	47.731	8.164	5.836	0.000	73.085
1	45.643	4.757	9.594	0.347	
	42.014	5.221	8.047	0.392	93.021
	20.700	9.140	2.264	0.000	85.441
2	33.642	20.981	1.603	0.161	
	59.562	12.955	4.597	0.392	97.730
	55.055	11.313	4.866	0.000	85.761
3	76.944	10.517	7.316	0.368	
	59.562	12.955	4.597	0.214	98.343
	29.289	24.258	1.207	0.000	91.036
4	43.800	4.826	9.074	0.108	
	41.484	4.923	8.426	0.035	94.364
	41.484	4.923	8.426	0.000	92.681
5	58.967	13.831	4.263	0.508	
	80.351	9.829	8.174	0.482	95.809
	45.755	14.758	3.100	0.000	83.258
6	44.991	35.160	1.280	-0.419	
	42.576	34.964	1.217	-0.485	99.276
	62.688	28.045	2.235	0.000	81.876
7	32.610	3.369	9.678	0.621	
	25.453	3.998	6.366	0.482	98.003
	19.285	4.721	4.084	0.000	83.340
8	41.325	34.624	1.194	0.581	
	42.576	34.964	1.217	0.607	98.343
	66.466	15.126	4.394	0.000	81.227
9	32.908	3.897	8.443	0.405	
	29.115	4.240	6.866	0.303	94.693
	32.908	4.685	7.024	0.000	86.833

Table 4.1: Injection parameters chosen at random to compare to the IMRSA spinning template bank, "Inj" refers to the injection and "S Temp" refers to the spinning template that best overlaps the injection; whereas, "NS Temp" refers to the nonspinning template that best overlaps the injection.

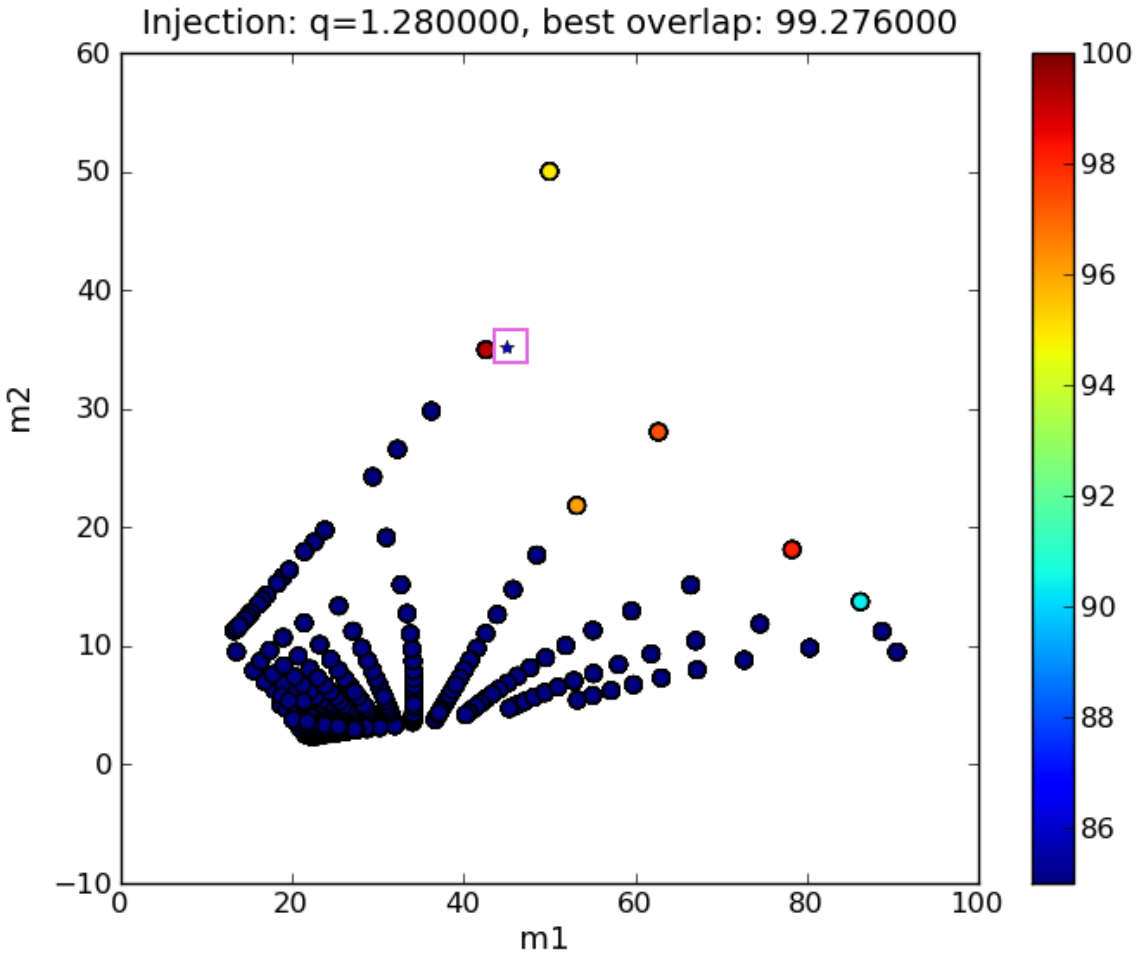

Figure 4.2: Representative plot of the overlap between the template bank and 10 random injections; specifically, the results from injection six in Table 4.1. The injection is shown as a star inside a box on the plot. The other points in the graph are from the IMRSA template bank generated in the method described above. The plot shows that in the m_1-m_2 plane the injection has high overlaps, indicated by circles of dark red color, with templates near to it.

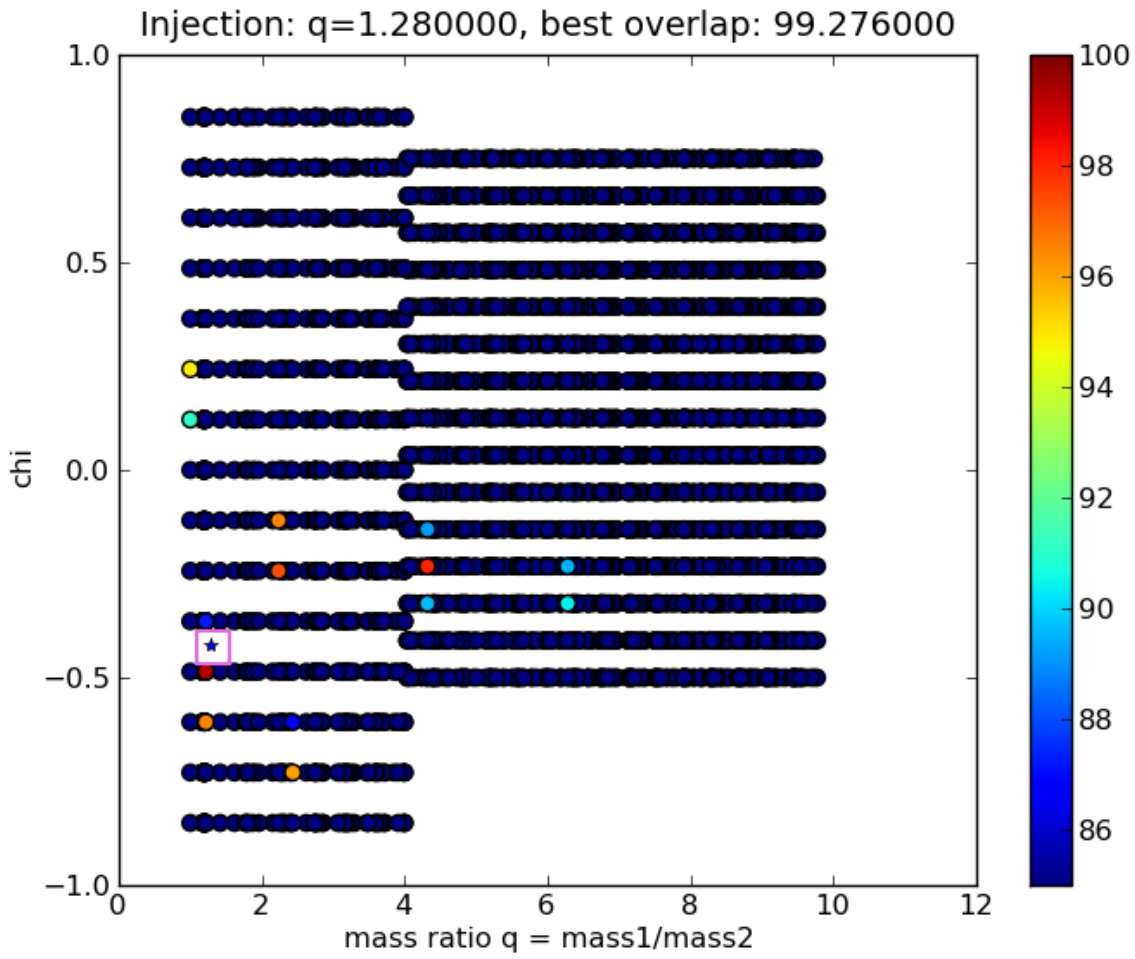

Figure 4.3: Representative plot of the overlap between the template bank and 10 random injections; specifically, the results from injection six in Table 4.1. The injection is shown as a star inside a box on the plot. The other points in the graph are from the IMRSA template bank generated in the method described above. The plot shows that in the χ-q plane the injection has high overlaps with templates within a range of about 1.0 around the injected χ value, with better placement schemes this window may be reduced.

Chapter 5

Results and Conclusions

The template banks described above were used to generate search templates in the *gstlal* inspiral pipeline, *lloid*, on the NINJA2 Test2 two week Gaussian noise data set. This dataset contains two weeks of colored Gaussian noise with injections of numerical relativity waveforms modeling non-precessing systems. The *lloid* pipeline does not yet calculate coincidence amongst the different detectors. Since the injections were made into Gaussian noise, glitches and other random noise in the detectors normally eliminated by coincidence tests are not present in the data rendering coincidence tests unnecessary. Several other searches were also run on this dataset by members of the NINJA2 collaboration, [35].

The results of the IMRSA search were compared to the results of running the *ihope* highmass nonspinning search, which used EOBNR templates on the two week Gaussian data set. The highmass search is described in [40]. The data sets were constructed such that each interferometer could be ana-

lyzed separately. As a result, coincidence tests were not run for the highmass search on these datasets. Direct comparisons can be made between the high-mass search and the IMRSA template bank results.

Additionally, I analyzed the NINJA2 two week Gaussian noise dataset with IMRSA templates where all the templates were assigned zero spin and were analyzed using *lloid*; this is referred to below as the IMRSA nonspinning search. Comparisons between the results with the spin turned on and turned off reinforces that differences seen between the spinning search and the nonspinning searches are a result of the inclusion of spin in the template banks.

5.1 Results

5.1.1 Comparative Efficiencies

Found and missed plots give an idea of how well a search does at recovering test signals, injections. The points on these graphs can fall into one of two categories, found or missed, but each category has two subclasses, see Table 5.1. When an injection does not fall into the subclass expected, then it provides information about possible problems with the pipeline or with the data, e.g. glitches.

For small numbers of injections like the number in the NINJA2 dataset, 101 in total, found and missed plots give a rough, qualitative idea of the efficiency of a search. Efficiency is how well a search returns a signal when one is present in the data. When viewed in comparison to another search run

on the same small set of injections made into the same data, these plots can be used to estimate how the two efficiencies compare. More rigorous tests, like receiver operator curves requiring large injection sets are needed obtain quantitative results.

Found AND expected	Found, NOT expected
Missed AND expected	Missed, NOT expected

Table 5.1: Often one has a sense of whether an injection should be found or not. When looking at a found/missed plot, every injection falls into one of the four categories above where expect means either "expected to be found" or "expected to be missed". The goal is to have all the injections be in the left hand column of the table; that is returned either found or missed as expected. An example of an injection one would expect to miss is one modeling a signal whose source is too distant to be seen by the detector. Injections falling into the right hand column provide insight into possible problems with the detection pipeline or the detector, and build intuition about future injection sets. In the plots that follow, found injections are represented by blue circles and missed injections by red crosses.

The plots in Figures 5.1 and 5.2 are labeled by interferometer, ifo. The notation for the ifo names is: *H1* is the Hanford, WA LIGO detector, *L1* is the Livingston, LA LIGO detector, and *V1* is the Pisa, Italy Virgo detector. The top plot in both Figures 5.1 and 5.2 are the result from *L1*, the bottom plot is the result from *V1*, and the *H1* efficiency plots are not shown as they are identical to each other in all three searches.

Figures 5.1 and 5.2 show the found and missed plots from running the spinning IMRSA search on the two weeks of NINJA2 Gaussian noise frames. In both figures the filled shapes indicate injections with different status in different searches. The plots in Figure 5.1 show the results from the spinning IMRSA template bank search compared to the nonspinning S5 highmass search results. The solid circles are injections missed by the spinning IMRSA template bank search but found in the nonspinning S5 highmass search for both the top and bottom plots in Figure 5.1, for more details on the S5 highmass search please see [40]. There were no injections found by the spinning IMRSA search that were missed by the highmass search. Additionally the efficiencies in *H1* from the spinning IMRSA search and the nonspinning highmass search were exactly the same (had exactly the same found/missed behavior) so no plots are shown for *H1*.

The plots in Figure 5.2 compare the results from the spinning IMRSA template bank search against those from the nonspinning IMRSA search. In this case the spinning IMRSA template bank was more efficient in detector *L1* but less efficient in *V1*. In each case the difference was in only one injection. The filled square in the top plot of Figure 5.2 is the injection found by the spinning IMRSA template bank search but missed by its nonspinning counterpart. In the bottom plot of Figure 5.2, the filled circle is an injection missed by the spinning IMRSA template bank search and found by its nonspinning counterpart. In *H1*, the efficiencies for the nonspinning and spinning IMRSA searches were the same so those plots are omitted. In *L1*, no injections were

found by the nonspinning IMRSA search and missed in the spinning IMRSA search, while in *V1*, no injections were found by the spinning IMRSA search that were missed by the nonspinning IMRSA search.

The essential feature of these plots is that the graphs for the IMRSA search and the graphs for the standard highmass search are nearly identical in *L1* and *V1* and *are* identical in *H1*. That they are not exactly the same is not disheartening as some differences are expected as effective distance is affected by quantities such as orientation of the source to the detector, the inclination angle between the source and the detector and the sky position of the source. The efficiencies obtained indicate comparable injection recovery between the highmass search and the spinning IMRSA search. Considering the ad-hoc placement of the IMRSA templates when constructing the corresponding banks, it is an amazingly good result with room for improvement. The dataset is small with only 101 injections; the plots indicate that the IMRSA spinning template bank search may be as efficient as the standard non-spinning search in this mass range though with the small number of injections made no hard statistics can be calculated. As is the efficiency of the spinning search versus the nonspinning searches gives no reason to use one over the other.

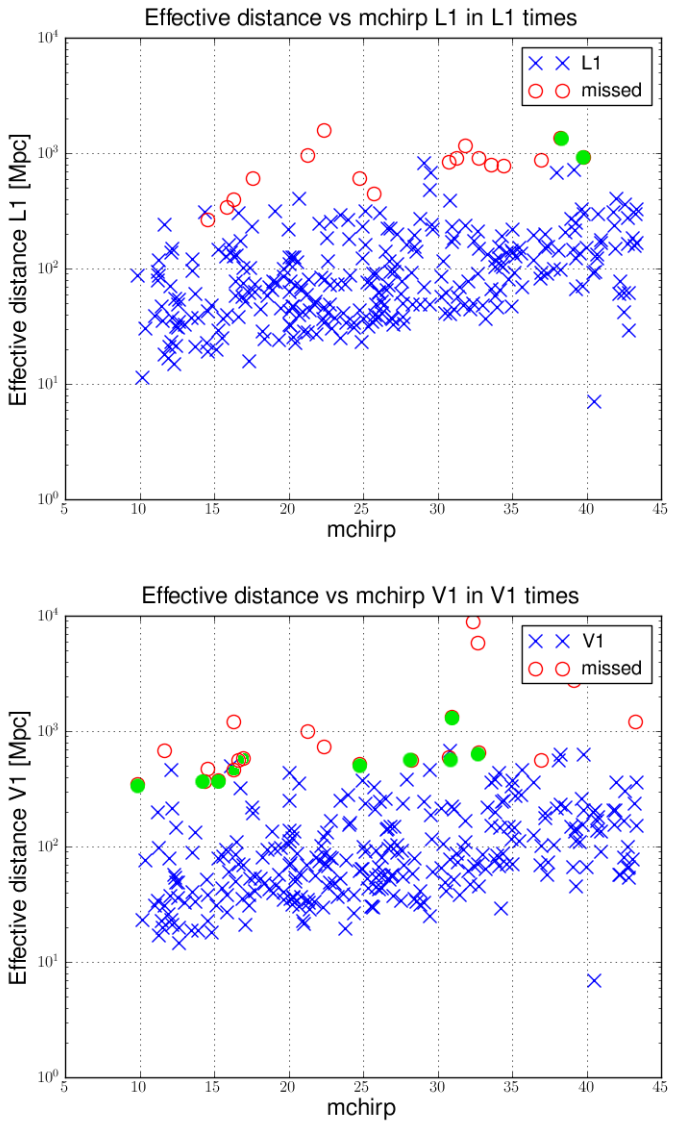

Figure 5.1: The found-missed plot for the injections displaying the chirp mass of the injection on the x-axis and the effective distance of the injection on the y-axis. The top plot is for *L1* from the spinning IMRSA template bank search. The bottom plot is for *V1* from the spinning IMRSA template bank search. The empty circles are the missed injections. The crosses are the found injections. This search is compared to the nonspinning highmass search. The filled circles represent injections found by the standard non- spinning highmass search and missed by the spinning IMRSA template bank search. *H1* results are omitted as the two searches were equally efficient.

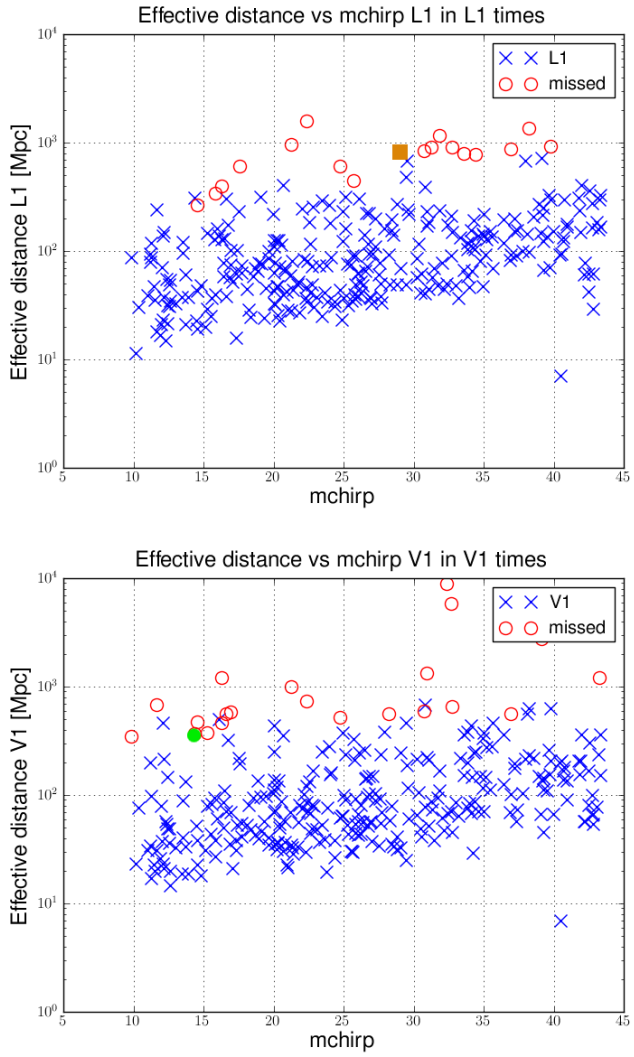

Figure 5.2: The found-missed plot for the injections displaying the chirp mass of the injection on the x-axis and the effective distance of the injection on the y- axis. The top plot is for *L1* from the spinning IMRSA search. The bottom for *V1* from the spinning IMRSA search. The empty circles are the missed injections. The crosses are the found injections. This search is compared to the nonspinning IMRSA search. In the top plot the filled square is an injection found by the spinning IMRSA template bank search but missed by the nonspinning IMRSA template bank search. In the bottom the filled circle is an injection missed by the spinning IMRSA template bank search but found by the nonspinning IMRSA template bank search. *H1* results are omitted as the two searches were equally efficient.

5.1.2 Parameter Recovery

Parameter recovery plots demonstrate how well we can determine the specifications of the signal. The CBC search operates with a focus on detecting whether a signal is present or not in the data, not with a focus on detecting the specific parameters of a signal. Parameter estimation is conducted after a possible signal is selected from the background data. The process is discussed in [46]. Nonetheless, improved recovery of the parameters of a signal before the parameter estimation step helps both in determining if the event is a true signal and in determining the correct specifications of the source later.

The search outlined above with IMRSA templates performs better at parameter recovery than the standard highmass search, see Figures 5.3, 5.4, 5.5. In fact, comparing the results from the highmass search and from the IMRSA template bank search with and without spin, shows a marked improvement in parameter recovery with the IMRSA spinning template bank. The results show the subtantially same improvements in all three detectors therefore only the results from *H1* are shown.

The SNR recovery plots, Figure 5.3, with spin show a stronger correlation between the injected and recovered values than seen without spin; therefore, the likelihood of properly recovering the SNR is higher for templates with spin. Proper recovery of SNR allows for better understanding of the source of the trigger. Glitches, SNR spikes related to problems with the detector, are associated with SNR much larger than the expected SNR of true signals. Therefore, improving the SNR recovery aids in sorting real signals

from noise and fake ones.

The chirp mass (mchirp) recovery plots, in 5.4, also improve with the addition of spin over the standard highmass search and the nonspinning IMRSA template bank search. Mchirp, is a combination of the masses that appears in the quadrupolar formulation of the period of two inspiraling compact binary objects, see Section 1.3.

Chirp mass recovery is especially difficult for higher mass systems as they are only in LIGO's frequency sensitivity range for a few cycles, which limits the effectiveness of the matched filtering algorithm. Therefore as mchirp increases, the correlation between recovered and injected values is expected to decrease. What spin gains you is a delay in when the correlation begins to fall apart. Instead of it deteriorating around an mchirp of $15M_{\odot}$, the correlation remains until roughly $25M_{\odot}$ and the spread above $25M_{\odot}$ is narrower with spin than without spin.

The horizontal lines seen in the mchirp recovery for IMRSA template banks' results are explained by how the template banks are calculated. In the IMRSA search, fixed template banks are used for the whole two weeks. In the highmass search, a new bank is generated every 2048s containing slightly different templates. As a result, a wider range of mass pairs are available in the highmass search and the lines are not visible in Figure 5.4.

The combined spin, χ, recovery plots are only shown for the spinning bank in Figure 5.5. Perhaps one of the most exciting results presented in this dissertation is that there is a correlation between the recovered and injected

χ values for the spinning IMRSA templates. This is a result not previously seen in any LIGO search as all previous search have used only non-spinning templates.

The IMRSA waveforms are an approximation to the signals injected into the NINJA2 datasets; there was a possibility that they would not capture the character of the spinning effects on the waveform. These plots show that they do capture it. Improvements in the bank may clean up the spin recovery and move it closer to the relation seen in the SNR plots. However, that the IMRSA search detects the fact that the component masses of a source are spinning, and distinguishes systems with spins aligned or anti-aligned with the total angular momentum from each other (positive or negative χ respectively), and even obtains the value within some error (to be calculated at a future date) represents a major step towards detection. Most CBC sources are believed to be spinning and there are arguments, based on tidal torquing, suggesting that spin aligned systems predominant over anti-aligned ones. So the ability to measure the spin of even this small subset of systems improves LIGO's ability to see gravitational waves from CBC sources like binary black holes.

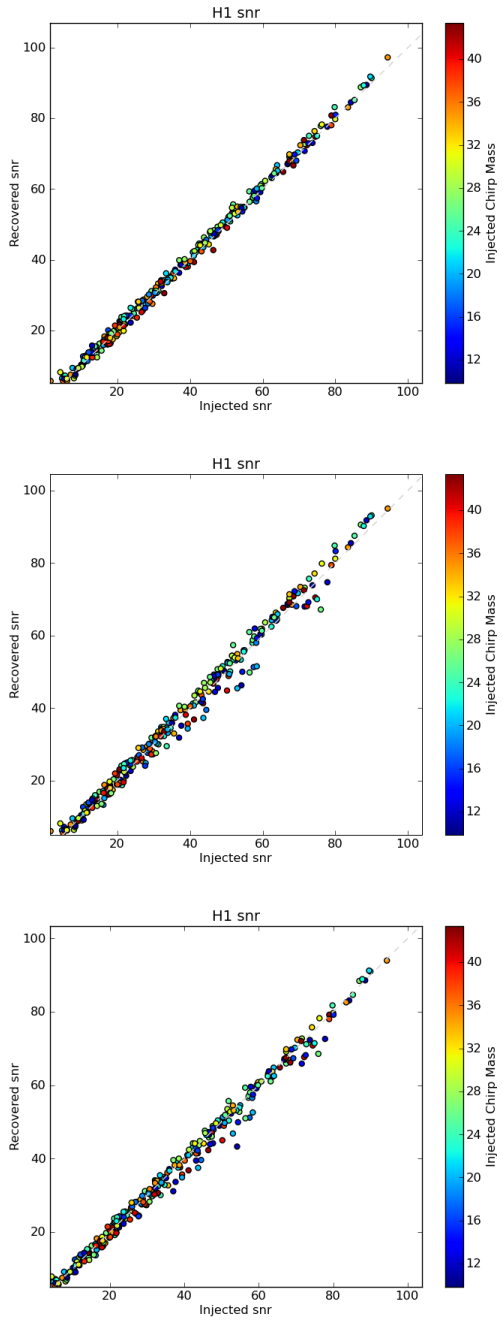

Figure 5.3: The SNR recovery: top, the spinning IMRSA template bank search; middle, the nonspinning highmass search; bottom the nonspinning IMRSA template bank search. Only *H1* results are shown as the results in *L1* and *V1* show the same improvements as seen in *H1*.

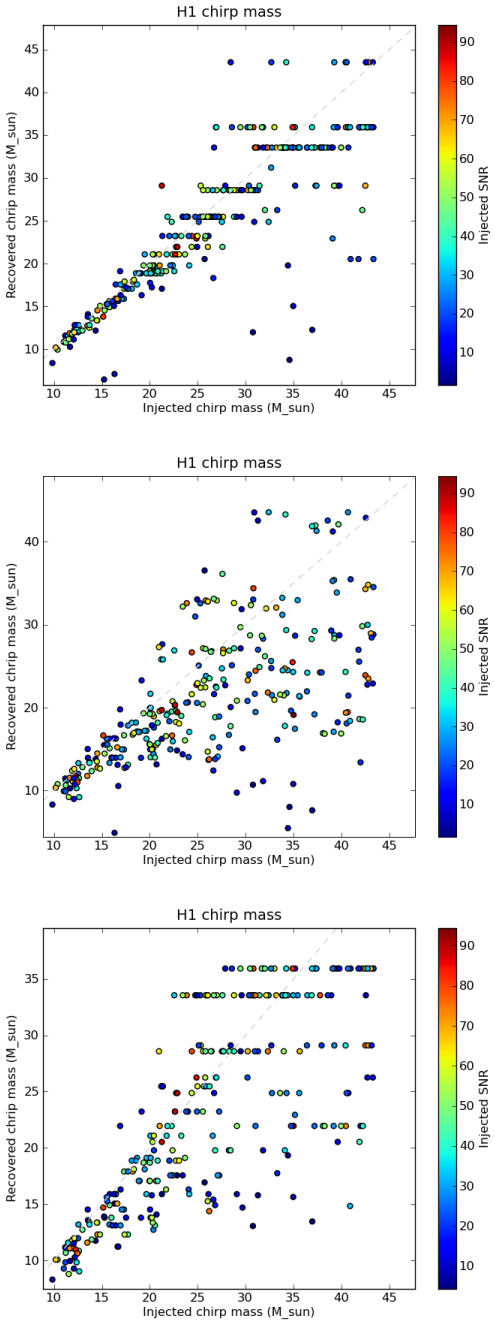

Figure 5.4: The mchirp recovery: top, the spinning IMRSA template bank search; middle, the nonspinning highmass search; bottom the nonspinning IMRSA template bank search. Only results from *H1* are shown. The same improvements are seen in all three interferometers.

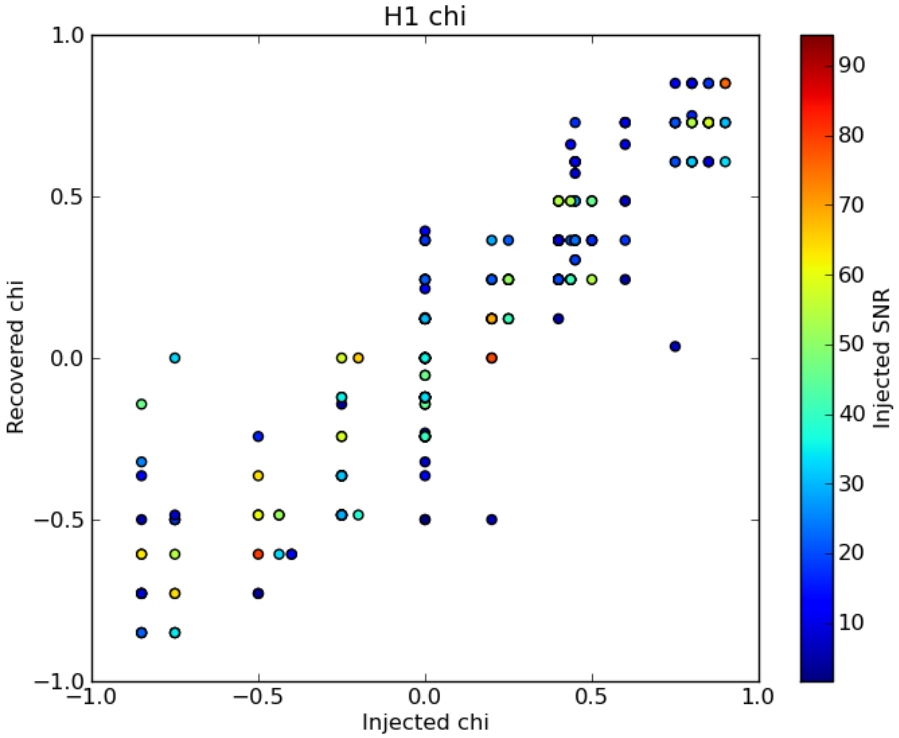

Figure 5.5: The combined spin, χ, recovery from the spinning IMRSA template bank search. The same correlation is seen in all three detectors so only the *H1* results are shown.

5.2 Conclusions

This dissertation shows that a search for compact binary coalescent systems, specifically binary black holes in the 35-100 $M_{\odot}$ range, would be improved by the use of IMRSA templates with the *lloid* pipeline. The search would then be able to discriminate between those sources where the component masses are not spinning and those where the spins are aligned or anti-aligned with the total orbital angular momentum.

When a search with IMRSA templates was compared to a search with non-spinning templates, either the EOBNR templates used in the S5 highmass search or the nonspinning IMRSA template bank search, on the same two weeks of colored Gaussian noise with numerically generated injections, the two searches found the injections with almost exactly the same efficiency. The two week sample is too small a set to quantitatively measure search efficiency; however, a run on the recently released two month Gaussian noise set is in progress; also a search using real noise is still pending. My results indicate that such further tests will show the spinning and nonspinning searches to be about as efficient as each other.

Where the IMRSA templates truly win over the nonspinning searches is in the parameter recovery. With IMRSA templates, it is easier to identify the characteristics of the numerical injection that created them. Since numerical injections model real signals, being able to more accurately return the parameters of such an injection implies that the template will better estimate those of a real signal. Therefore using IMRSA templates on real data will increase

the likelihood of identifying a gravitational wave event and later identifying its source.

The IMRSA templates like those used here allow for the exploration of the spin parameter space. Other spinning template families to explore include the IMRSA templates described in [58]. The aligned or anti-aligned case is a small step towards a fully spinning search. Non aligned spins will cause the waveform to precess; precessing waveforms are difficult to model and are computationally very expensive to numerically produce. A search including precessing templates is much more complex and computationally challenging enterprise than the spin aligned case. Here I demonstrate a way to differentiate between spinning systems with aligned and those with anti-aligned spinning systems, and to estimate the total spin of the system. This capability increases LIGO's ability to detect gravitational waves from binary black hole mergers. I conclude that a search with IMRSA templates should be taken to the next step in LIGO/Virgo Compact Binary Coalescence searches and developed to run on real data like that of S5 or subsequent science runs like S6 and beyond.

Bibliography

[1] A. Buonanno and T. Damour, Phys. Rev. D 59, 084006 (1999). URL: http://arxiv.org/pdf/gr-qc/9811091v1

[2] A. Buonanno and T. Damour, Phys. Rev. D 62, 064015 (2000).

[3] A. Buonanno et al., Phys. Rev. D 76, 104049 (2007).

[4] A. Buonanno, Y. Chen, and T. Damour, Phys. Rev. D 74, 104005 (2006).

[5] A. Sadowski, K. Belczynski, T. Bulik, N. Ivanova, F. A. Rasio, and R. O'Shaughnessy, Astrophys. J. 676, 1162 (2008).

[6] B. J. Owen, Phys. Rev. D 53, 6749 (1996).

[7] B. Brugmann, J. A. Gonzalez, M. Hannam, S. Husa, U. Sperhake, and W. Tichy, Phys. Rev. D 77, 024027 (2008).

[8] B P Abbott et al 2009 Rep. Prog. Phys. 72 076901

[9] Blandford, R., and Teukolsky, S.A.,"Arrival-time analysis for a pulsar in a binary system", Astrophys. J., 205, 580-591, (1976).

[10] Bruce Allen, Warren G. Anderson, Patrick R. Brady, Duncan A. Brown, and Jolien D. E. Creighton, "FINDCHIRP: an algorithm for detection of gravitational waves from inspiraling compact binaries", arXiv:gr-qc/0509116v1.

[11] B. Sathyaprakash and B. Schutz, Liv. Rev. Relativity 12 (2009).

[12] B S Sathyaprakash and V S Dhurandhar, Phys. Rev. D 44, 3819 (1991).

[13] Burke, W.L., "Gravitational Radiation Damping of Slowly Moving Systems Calculated Using Matched Asymptotic Expansions", J. Math. Phys., 12, 401-418, (1971).

[14] C. A. K. Robinson, B. S. Sathyaprakash and Anand S. Sengupta Phys. Rev. D 78, 062002 (2008).

[15] C. F. Gammie et al., Astrophys. J. 602, 312 (2004).

[16] Chandrasekhar, S., and Esposito, F.P., "The $2\frac{1}{2}$-Post-Newtonian Equations of Hydrodynamics and Radiation Reaction in General Relativity", Astrophys. J., 160, 153-179, (1970).

[17] Cokelaer, T. Phys. Rev. D 76, 102004 (2007).

[18] Damour, T., and Taylor, J.H., "On the orbital period change of the binary pulsar PSR 1913+16", Astrophys. J., 366, 501-511, (1991).

[19] Diego Fazi. "Development of a physical-template search for gravitational

waves from spinning compact-object binaries with LIGO". PhD disseration, Universita di Bologna, 2009.

[20] D. Pollney et al., Phys. Rev. D 76, 124002 (2007).

[21] Duncan Brown, Searching for Gravitational Radiation from Binary Black Hole MACHOs in the Galactic Halo. arXiv:0705.1514.

[22] E. T. Newman and R. Penrose, J. Math. Phys. (N.Y.) 3, 566 (1962); 4, 998(E) (1963).

[23] Einstein, A., "Explanation of the Perihelion Motion of Mercury from the General Theory of Relativity", Sitzungsber. Preuss. Akad. Wiss., 1915, 831-839, (1915).

[24] A Einstein, Infeld, Hoffmann,"The Gravitational Equations and the Problem of Motion", Ann. Math., 39, 65-100, (1938).

[25] Epstein, R., "The binary pulsar: Post-Newtonian timing effects", Astrophys. J., 216, 92-100, (1977). Related online version: http://adsabs.harvard.edu/abs/1977ApJ...216...92E

[26] "FINDCHIRP: an algorithm for detection of gravitational waves from inspiraling compact binaries", Bruce Allen, Warren G. Anderson, Patrick R. Brady, Duncan A. Brown, Jolien D. E. Creighton gr-qc/0509116 (September 2005).

[27] F. Echeverria, Phys. Rev. D 40, 3194 (1989).

[28] F. Ozel, D. Psaltis, R. Narayan, and J. E. McClintock, Astrophys. J. 725, 1918 (2010).

[29] Frans Pretorius, "Evolution of Binary Black-Hole Spacetimes", PRL 95, 121101 (2005).

[30] Gian Mario Manca and Michele Vallisneri, "Cover art: Issues in the metric-guided and metric-less placement of randomand stochastic template banks", Phys. Rev. D 81, 024004 (2010), arXiv:0909.0563v2[gr-qc] 14Jan2010.

[31] H. A. Lorentz and J. Droste, Versl. K. Akad. Wet. Amsterdam 26, 392, 649 (1917); H. A. Lorentz J. Droster, The Collected Papers of H. A. Lorentz (Nijhoff, The Netherlands, 1937), Vol. 5, p. 330.

[32] http://www.gstreamer.net/

[33] https://www.lsc-group.phys.uwm.edu/daswg/projects/gstlal.html.

[34] https://www.lsc-group.phys.uwm.edu/daswg/projects/lalsuite.html.

[35] https://www.ninja-project.org/doku.php.

[36] Hulse, R.A., and Taylor, J.H., "Discovery of a pulsar in a binary system", Astrophys. J. Lett., 195, L51-L53, (1975).

[37] Ian Hinder 2010 Class. Quantum Grav. 27 114004 doi: 10.1088/0264-9381/27/11/114004.

[38] I. W. Harry, B. Allen, and B. S. Sathyaprakash,"Stochastic template placement algorithm for gravitational wave data analysis", Phys. Rev. D 80, 104014 (2009), arXiv:0908.2090v1[gr-qc]14Aug2009.

[39] J. A. Orosz, J. E. McClintock, R. Narayan, C. D. Bailyn, J. D. Hartman, L. Macri, J. Liu, W. Pietsch, R. A. Remillard, A. Shporer et al., Nature (London) 449, 872 (2007).

[40] J. Abadie, et al, "Search for gravitational waves from binary black hole inspiral, merger, and ringdown", Phys. Rev. D 83, 122005 (2011), http://link.aps.org/doi/10.1103/PhysRevD.83.122005.

[41] J. Abadie, et al., Class. Quantum Grav. (2010) 173001.

[42] J. M. Bardeen et al., Astrophys. J. 178, 347 (1972).

[43] J. M. Stewart, Advanced General Relativity (Cambridge University Press, Cambridge, 1990).

[44] J. M. Weisberg and J. H. Taylor. The Relativistic Binary Pulsar B1913+16: Thirty Years of Observations and Analysis. In Binary Radio Pulsars, ASP Conference Series, Vol. 328, Proceedings of the conference held 11-17 January, 2004, Aspen, Colorado, USA. Edited by F. A. Rasio and I. H. Stairs. San Francisco: Astronomical Society of the Pacific, 2005., p.25.

[45] Jinho Kim, "General Relativistic Hydrodynamics Using BSSN formalism", http://www.ksc.re.kr/kcnr/Presentations/26thNR/26thNRJKim.pdf.

[46] J. Veitch and A. Vecchio, Phys. Rev. D. 81 6 062003.

[47] K. Belczynski et al., Astrophys. J. 714, 1217 (2010).

[48] K. Belczynski, M. Dominik, T. Bulik, R. O'Shaughnessy, C. Fryer, and D. E. Holz, Astrophys. J. 715, L138 (2010).

[49] K. G. Arun et al., Phys. Rev. D 79, 104023 (2009).

[50] Kipp Cannon, Adrian Chapmen, Chad Hanna, Drew Keppel, Anony C. Searle and Alan J. Weinstein arXiv:1005.0012v1 [gr-qc] 30 Apr 2010.

[51] Kipp Cannon, Romain Cariou, Adrian Chapman, Mireia Crisp'n-Ortuzar, Nickolas Fotopoulos, Melissa Frei, Chad Hanna, Erin Kara, Drew Keppel, Laura Liao, Stephen Privitera, Antony Searle, Leo Singer, Alan Weinstein, http://arxiv.org/abs/1107.2665

[52] Kipp Cannon, Chad Hanna, Drew Keppel, and Antony C. Searle, Phys. Rev. D 83, 084053 (2011).

[53] Kipp Cannon, Chad Hanna, Drew Keppel, "Efficiently enclosing the compact binary parameter space by singular-value decomposition," arXiv:1101.4939v1 [gr-qc]

[54] L. Blanchet, G. Faye, B. R. Iyer, and S. Sinha, Class. Quant. Grav. 25, 165003 (2008), ISSN 0264-9381, URL http://stacks.iop.org/0264-9381/25/i=16/a=165003.

[55] Lawrence E Kidder, Clifford M Will and Alan G Wiseman, Class Quantum Grav. 9 (1992) Ll25-L131.

[56] LIGO-G060009-03, https://dcc.ligo.org/public/0036/G060009/000/G060009-03.pdf.

[57] Living Rev. Relativity, 10, (2007), 2 http://www.livingreviews.org/lrr-2007-2

[58] L. Santamaria, F. Ohme, P. Ajith, B. Brugmann, N. Dorband, M. Hannam, S. Husa, P. Mosta, D. Pollney, C. Reisswig, E. L. Robinson, J. Seiler, and B. Krishnan, "Matching post-Newtonian and numerical relativity waveforms: Systematic errors and a new phenomenological model for nonprecessing black hole binaries", Phys. Rev. D 82, 064016 (2010).

[59] Luc Blanchet et al 1996 Class. Quantum Grav. 13 575 doi: 10.1088/0264-9381/13/4/002.

[60] Luc Blanchet, Guillaume Faye, Bala R. Iyer, and Benoit Joguet, "Gravitational-wave inspiral of compact binary systems to $\frac{1}{2}$ post-Newtonian order", Phys. Rev. D,65, 061501 R, URL: http://arxiv.org/pdf/gr-qc/0001013v2.

[61] L. Blanchet, G. Faye, B. R. Iyer, and S. Sinha, Class. Quant. Grav. 25, 165003 (2008), ISSN 0264-9381, URL http://stacks.iop.org/0264-9381/25/i=16/a=165003.

[62] M. Volonteri et al., Astrophys. J. 620, 69 (2005).

[63] M. Campanelli, C. O. Lousto, P. Marronetti, and Y. Zlochower, "Accurate Evolutions of Orbiting Black-Hole Binaries without Excision", PRL 96, 111101 (2006). http://prl.aps.org/pdf/PRL/v96/i11/e111101.

[64] P. Ajith et al., Phys. Rev. D 77, 104017 (2008), URL: arXiv:0710.2335.

[65] P. Ajith, et. al. arXiv:0909.2867v1 [gr-qc] 15 Sep 2009.

[66] P. Ajith, et. al., "Data formats for numerical relativity", arXiv:0709.0093v3 [gr-qc]

[67] P. Ajith, M. Hannam, S. Husa, Y. Chen, B. Brugmann, N. Dorband, D. Muller, F. Ohme, D. Pollney, Reisswig, L. Santamaria, and J. Seiler, "Inspiral-Merger-Ringdown Waveforms for Black-Hole Binaries with Non-precessing Spins", PRL 106, 241101 (2011). URL: http://arxiv.org/pdf/0909.2867v2.

[68] P. Ajith, S. Babak, Y. Chen, M. Hewitson, B. Krishnan, A. M. Sintes, J. T. Whelan, B. Brugmann, P. Diener, N. Dorband, J. Gonzalez, M. Hannam, S. Husa, D. Pollney, L. Rezzolla, L. Santamaria, U. Sperhake, and J. Thornburg, "Template bank for gravitational waveforms from coalescing binary black holes: Nonspinning binaries", Phy. Rev. D 77, 104017 (2008).

[69] P. D. Welch, IEEE Trans. Audio Electroacoust., AU-15, 70, (1967).

[70] Parameswaran Ajith, Kipp Cannon, Britta Daudert, Melissa Frei, Chad Hanna, Shaun Hooper, Drew Keppel, Adam Mercer, Stephen Privitera, Antony Searle, Leo Singer, "gstlal: A stream-based approach to data analysis", LIGO-DCC: G1000153-v2, unpublished talk.

[71] "Proposal for NINJA-2," Ajith et. al (the NINJA-2 collaboration), https://www.ninja-project.org/lib/exe/fetch.php?media=ninja2:ninjasciencecase.pdf.

[72] P. Grandclement et al., Phys. Rev. D 69, 102002 (2004).

[73] R. A. Remillard and J. E. McClintock, Annu. Rev. Astron. Astrophys. 44, 49 (2006).

[74] R. O'Shaughnessy, V. Kalogera, and K. Belczynski, Astrophys. J. 716, 615 (2010).

[75] S. Babak, Balasubramanian, D. Churches, T. Cokelaer, and B. Sathyaprakash, Classical Quantum Gravity 23, 5477 (2006).

[76] S. L. Shapiro, Astrophys. J. 620, 59 (2005).

[77] T. Bogdanovic et al., Astrophys. J. 661, L147 (2007).

[78] T. Bulik and K. Belczyn«ski, Astrophys. J. 589, L37 (2003).

[79] T. Bulik, K. Belczynski, and A. Prestwich, Astrophys. J. 730, 140 (2011).

[80] V. Kalogera, Pramana 63, 673 (2004).

[81] W. H. Press, S. A. Teukolsky, W. T. Vetterling, and B. P. Flannery, Numerical Recipes in C: the art of scientiÞc computing, 2nd ed. (Cambridge University Press, Cambridge, 1992) Section 13.4

[82] Will, C.M., "Experimental gravitation from NewtonÕs Principia to EinsteinÕs general relativity", in Hawking, S.W., and Israel, W., eds., Three Hundred Years of Gravitation, 80-127, (Cambridge University Press, Cambridge, U.K.; New York, U.S.A., 1987).

[83] Will, C.M., Theory and experiment in gravitational physics, (Cambridge University Press, Cambridge, U.K.; New York, U.S.A., 1993), 2nd edition.

[84] Will, C.M., "Gravitational Waves from Inspiraling Compact Binaries: A Post-Newtonian Approach", in Sasaki, M., ed., Relativistic Cosmology, Proceedings of the 8th NishinomiyaYukawa Memorial Symposium, Shukugawa City Hall, Nishinomiya, Hyogo, Japan, 28 - 29 October, 1993, vol. 8 of NYMSS, 83-98, (Universal Academy Press, Tokyo, Japan, 1994). Related online version: http://arXiv.org/abs/gr-qc/9403033.

[85] Will, C.M., "The Confrontation between General Relativity and Experiment", Living Rev. Relativity, 9, lrr-2006-3, (2006). URL: http://www.livingreviews.org/lrr-2006-3.

[86] W. M. Farr, N. Sravan, A. Cantrell, L. Kreidberg, C. D. Bailyn, I. Mandel, and V. Kalogera, arXiv:1011.1459.

[87] Y. Pan, A. Buonanno, L. T. Buchman, T. Chu, L. E. Kidder, H. P. Pfeiffer, and M. A. Scheel, Phys. Rev. D 81, 084041 (2010). URL: http://arxiv.org/pdf/0912.3466v2.

Vita

Melissa Frei was born in Baldwinsville, New York to John and Arlene Frei. She attend C.W. Baker High School in Baldwinsville, New York, eventually attending college at Syracuse University, where she graduated Magna Cum Laude, a Sigma Pi Sigma member and a Golden Key International member with a B.S. in Physics. She has a passion for art along with science and sees the two as fundamentally based on problem solving.

Permanent Address: 8435 Transit Ln

Baldwinsville, NY 13027

This dissertation was typeset with LaTeX 2_ε[1] by the author.

[1] LaTeX 2_ε is an extension of LaTeX. LaTeX is a collection of macros for TeX. TeX is a trademark of the American Mathematical Society. The macros used in formatting this dissertation were written by Dinesh Das, Department of Computer Sciences, The University of Texas at Austin, and extended by Bert Kay, James A. Bednar, and Ayman El-Khashab.